Journal Pre-proofs

Electron Tomography Reveals Changes in Spatial Distribution of UBTF1 and UBTF2 Isoforms within Nucleolar Components during rRNA Synthesis Inhibition

Pavel Tchelidze, Hervé Kaplan, Christine Terryn, Nathalie Lalun, Dominique Ploton, Marc Thiry

PII: S1047-8477(19)30184-4
DOI: https://doi.org/10.1016/j.jsb.2019.08.014
Reference: YJSBI 7383

To appear in: *Journal of Structural Biology*

Received Date: 5 July 2019
Revised Date: 29 August 2019
Accepted Date: 30 August 2019

Please cite this article as: Tchelidze, P., Kaplan, H., Terryn, C., Lalun, N., Ploton, D., Thiry, M., Electron Tomography Reveals Changes in Spatial Distribution of UBTF1 and UBTF2 Isoforms within Nucleolar Components during rRNA Synthesis Inhibition, *Journal of Structural Biology* (2019), doi: https://doi.org/10.1016/j.jsb.2019.08.014

Electron Tomography Reveals Changes in Spatial Distribution of UBTF1 and UBTF2 Isoforms within Nucleolar Components during rRNA Synthesis Inhibition.

Pavel Tchelidze[a], Hervé Kaplan[b], Christine Terryn[c], Nathalie Lalun[d], Dominique Ploton[e], Marc Thiry[f,g]

[a] Faculty of Health, Eastern European University, Tbilisi, Georgia

[b] Université de Reims Champagne Ardenne, Reims, France

[c] Platform of Cellular and Tissular Imaging (PICT), Université de Reims Champagne Ardenne, Reims, France

[d] UMR-S 1250 INSERM, Université de Reims Champagne Ardenne

[e] BioSpecT, EA 7506, Université de Reims Champagne Ardenne

[f] Unit of Cell and Tissue Biology, GIGA-Neurosciences, University of Liège, Liège, Belgium

[g] corresponding author: mthiry@uliege.be (MT)

Running head: 3D distribution of UBTF 1 and 2

Abbreviations used: AMD: actinomycin D; DFC: dense fibrillar component; EM: electron microscopy; FCs: fibrillar centers; NORs: nucleolar organizer regions; Pol I: RNA polymerase I; UBTF1/2: upstream binding transcription factor 1 or 2

Key words: UBTF1/2, electron tomography, fibrillar centers, rDNA, nucleolar caps, mitotic NORs, AMD.

Abstract

Upstream binding transcription factor (UBTF) is a co-regulator of RNA polymerase I by constituting an initiation complex on rRNA genes. UBTF plays a role in rDNA bending and its maintenance in "open" state. It exists as two splicing variants, UBTF1 and UBTF2, which cannot be discerned with antibodies raised against UBTF. We investigated the ultrastructural localization of each variant in cells synthesizing GFP-tagged UBTF1 or UBTF2 by using anti-GFP antibodies and pre-embedding nanogold strategy. Detailed 3D distribution of UBTF1 and 2 was also studied by electron tomography. In control cells, the two isoforms are very abundant within fibrillar centers, but their repartition strongly differs. Electron tomography shows that UBTF1 is disposed as fibrils that are folded in coils whereas UBTF2 is localized homogenously, preferentially at their cortical area. As UBTF is a useful marker to trace rDNA genes, we used these data to improve our previous model of 3D organization of active transcribing rDNA gene within fibrillar centers. Finally, when rRNA synthesis is inhibited during actinomycin D treatment or entry in mitosis, UBTF1 and UBTF2 show a similar distribution along extended 3D loop-like structures. Altogether these data suggest new roles for UBTF1 and UBTF2 isoforms in the organization of active and inactive rDNA genes.

Introduction

The nucleolus is the largest and densest membrane-less nuclear compartment where the molecular and structural factories of ribosome biogenesis are properly associated and tightly coordinated (Hernandez-Verdun *et al.,* 2010; Farley *et al.,* 2015). Plenty of structural and regulatory proteins, specifically linked to different steps of ribosome production are engaged in the dense packaging of the molecular constituents of the nucleolus (Andersen *et al.,* 2002, 2005). Ribosome biogenesis starts with the synthesis of pre-rRNA chain, a central event guided by the rDNA-dependent RNA-polymerase I (Pol I) in cooperation with a variety of accessory proteins (Pol I associated factors, PAFs) composing r-genes transcription machinery (Grummt, 2003; Moss, 2004; Thiry and Lafontaine, 2005; Stefanovsky *et al.,* 2006; Goodfellow and Zomerdjik, 2012). Next steps, including processing and maturation are required to form pre-ribosomal rRNP particles of different size, as well as final assembling of large and small ribosomal subunits are also under control of specific multi-protein assemblies, defined as rRNA processing and pre-ribosome formation machineries (Henras *et al.,* 2015). Hence, the nucleolus emerges due to presence of highly repeated and tandemly organized active rRNA genes array associated and surrounded with relevant protein machineries and products of their activity.

In mammals and man, transmission electron microscopy identifies four sub-compartments or nucleolar components (NCs) namely: (i) *fibrillar centers* (FCs); (ii) *dense fibrillar component* (DFC); (iii) *granular component* (GC) and (iv) *interstices or nucleolar vacuoles* (NVs) (Thiry and Goessens, 1996, Thiry and Lafontaine, 2005, Lamaye et al, 2011). In addition to nucleic acids, each NC contains a specific set of resident proteins that may be localized by using immunodetection or GFP-tagging (Thiry and Goessens, 1996, Krüger *et al.,* 2007). Being an interphase derivate of mitotic Nucleolar Organizer Regions (NORs), FCs represent sites of localization and transcription of non-nucleosomal rDNA loops (for a review see Derenzini et al. 2006). This is attested by the localization of major specific markers of r-chromatin inside FCs such as Pol I, UBTF, SL1, Topo I (Thiry and Goessens, 1996; Seither et al, 2001; Derenzini *et al.* 2006; Ponti et al, 2014). The transient area between FC and DFC is considered to contain transcriptionally active r-genes, from which the growing pre-rRNAs enter rapidly DFC (Cheutin *et al.,* 2002). However, some authors consider that active r-genes, together with linked Christmas tree segments, are localized in DFC (Koberna *et al.,* 2002, for review see Raska et al. 2004). The DFC

juxtaposed to FCs, corresponds to the nucleolar territory where early processing of nascent pre-rRNA takes place as confirmed by the localization of early processing markers such as fibrillarin, nucleolin (Krüger *et al.,* 2007). The more advanced steps of pre-rRNA maturation occur on the periphery of the DFC, whereas late processing and pre-ribosome assembling (specific markers: nucleolar proteins B23, NOP52; different ribosomal proteins) develop within nucleolar territory known as GC (Krüger *et al.,* 2007). The presence of small condensed chromatin blocks in nucleolar interstices, particularly those in contact with FCs, has been noted repeatedly by different cytochemical and immunocytological approaches (Thiry and Goessens, 1996; Thiry and Lafontaine, 2005). Most likely, interstices contribute to 3D organization of the intranucleolar condensed chromatin that can be visualized using histone H2B-GFP labeling (Tchelidze *et al.,* 2017).

For many years, the nucleolus has appeared as a paradigm for the study of molecular and structural organization of active genes, of their transcription and of their processing (Hernandez-Verdun *et al.,* 2010). To understand how the different players of the transcriptional machinery are organized within NCs, many efforts have been devoted to the analysis of the nucleolus within living or fixed cells by using cellular imaging (Thiry *et al.,* 1991; Scheer and Hock, 1999; Thiry *et al.,* 2000; Derenzini *et al.,* 2006; Tafforeau *et al.,* 2013; Nicolas *et al.,* 2016).

More particularly, the 3D organization of active or inactive rRNA genes is still under investigation. We previously described the 3D organization of active rDNA genes within FC by focusing on Pol I molecules (Cheutin *et al.,* 2002). To reach that goal, we localized Pol I molecules by using nanogold pre-embedding immunolabeling and we used electron tomography to study their 3D distribution within thick sections. This approach demonstrated a non-random 3D disposition of Pol I molecules within FC as coils and loops that we interpreted as the trace of active rDNA gene. We used these findings to propose the first model of the 3D organization of active rDNA genes within the cortex of FCs (Cheutin *et al.,* 2002). This model was recently modified by localizing the intergenic spacer of rDNA (IGS) within the more central part of FC (Denissov *et al.,* 2011).

To complete our model, we decided to investigate the 3D organization of another member of Pol I machinery, the *Upstream Binding Transcription Factor* (UBTF), an architectural PAF, essential to r-genes transcription (Cavanaugh *et al.,* 2003; Goodfellow and Zomerdjik, 2012; Hamdane *et al.,* 2014). It is now known that UBTF is associated only with r-gene enhancer region and transcription unit but not across the remaining part of the IGS (Hamdane *et al.,* 2014; Herdman et al, 2017; Moss et al, 2019). The main structural function of UBTF consists in maintaining rDNA chromatin in an open (i.e. non-nucleosomal or under-condensed) state as well as in formation of rDNA loops (Mais *et al.,* 2005; McStay, 2016; Mangan *et al.,* 2017). The looping of rDNA induces UBTF-dependent incorporation of other transcription factors at promoter site (Goodfellow and Zomerdjik, 2012). Moreover, inhibition of rDNA transcription does not affect UBTF-rDNA complex as UBTF retains association with inactive r-genes (Zatsepina *et al.,* 1993; Herdman et al, 2017).

Interestingly, UBTF consists of two splicing variants of different length, known as UBTF1 and UBTF2 (O'Mahony and Rothblum, 1991). UBTF1 has been shown to be a more potent activator of r-gene transcription comparatively to UBTF2 which is nonfunctional at the r-gene promoter due to a deletion of 37 amino acids of the second HMG box (Kuhn *et al.,* 1994). Meanwhile, UBTF1 seems to have a unique function, being involved in rDNA bending and formation of rDNA loops (Sanij *et al.,* 2008, 2015). Since UBTF1 and UBTF2 cannot be discerned by using antibodies raised against UBTF, we choose to specifically identify each variant in transiently transfected cells synthesizing either GFP-tagged UBTF1 or UBTF2 by using antibodies raised against GFP. We then used pre-embedding anti-GFP nanogold immuno-labeling subsequently amplified with silver: i) to precisely localize each isoform in the thickness of ultrathin sections and ii) to study their 3D distribution in thick sections by electron tomography (Cheutin *et al.*, 2002; Tchelidze *et al.,* 2006, 2008).

Here, these approaches were applied to answer the following questions concerning the localization of UBTF1 and UBTF2 isoforms: i) do they both localize within FC and if yes, ii) do they co-localize, iii) how data can be used to improve our previous model of rDNA 3D organization within FC, iv) do they show similar 3D disposition during active rRNA synthesis and during inactivation of rRNA synthesis induced by either AMD treatment or entry in mitosis.

Material and Methods

Cell culture and transfection technique

1) Properties of KB cells and cultivation/AMD treatment conditions

Experiments were conducted on KB human cancer cell line transiently transfected with UBTF1-GFP or UBTF2-GFP. The same nucleolus of control KB cells can contain FCs of different sizes: small FCs are 0.3 μm - 0.5 μm in diameter whereas large ones are 0.9 μm - 1.5 μm in diameter. It is important to note here that KB cells are misidentified HeLa cells (Vaughan *et al.,* 2017).

Cells were grown without antibiotics in DMEM containing a source of L-glutamine and 10% foetal bovine serum (Invitrogen, France). Cells were seeded at 5×10^4 cells/cm^2 on glass coverslips, and incubated at 37°C in an atmosphere enriched with 5% CO_2 for 24-36 h. Generally, cells were cultivated, reseeded, tested for mycoplasma detection as well as harvested and stored using the same conditions and protocols as in previous work (Tchelidze *et al.,* 2006). We inhibit rRNA synthesis with AMD (Merck, Germany). For this, both non-transfected and transfected cultures were treated with AMD dissolved in cultural media to reach the final concentration of 0.05 μg/ml. Cells were incubated in the antibiotic containing media during 1 h – 3 h. As an example of natural inactivation, we visualized the fibrillar structure of silenced r-chromatin during mitosis, that give the rise to small, medium and large metaphase NOR's.

Control and AMD-treated KB cells transfected for UBTF-GFP expression were fixed for 10 min in 4% paraformaldehyde (EMS, USA) and mounted in Citifluor AF1 (Agar Scientific, UK). Before EM analysis transfected cells (both control and AMD treated) were examined in LCM. Part of transfected cells was submitted to anti-GFP immuno-labeling and further observation in TEM and MV STEM (see below).

2) Engineering of the GFP fusion proteins and transfection technique

Total mRNAs were extracted from human KB cells with the PolyATtract system III (Promega, USA) and reverse-transcripted into cDNAs using the SuperScript kit (Invitrogen, France). Full-length clones of hUBF1 and hUBF2 were then PCR-amplified using the following oligonucleotides:

a) Sense, 5'-GGAACCGGTATGAACGGAGAAGCCGACTGCCCCACAG-3';
b) Antisense, 5'-CCAGGATCCTCCGGTGCTGGCTTAGTCTGATAGTTGCTGTCC-3'.

After a BspEI–BamHI digest, the PCR products were cloned into the *Age I* and *BamH I* sites of pEGFP-C1 vector (Clontech Laboratories, USA). The selected clones for UBF1 (pC45) and UBF2 (pB01) were sequenced on both strands to check the sequences.

Cells were transiently transfected with UBTF1-GFP or UBTF2-GFP according to the following protocol. Before transfection, cell suspension was placed in a plastic Petri dish (Nunclon, Denmark) onto Ø 4mm glass coverslips (Bioptech, USA) at the concentration of 5x10 cells/ cm² and allowed for 24-36h to reach 50-60% of confluence. Then the media was changed and 1μg of cDNA prepared in the form of plasmidic constructs coding for EGFP-UBF1 or EGFP-UBF2 fusion proteins was delivered to the cells by FuGene-6 (3:2 reagent to DNA, Roche Diagnostics, Switzerland) according to the manufacturer's instructions.

In special experiments the double transfection using plasmidic DNA constructed for UBTF1-GFP and UBTF2-DsRed fusion proteins was performed, according to the early described technique (Tchelidze et al., 2017). These double labeled samples were used as control for efficient co-localization between UBF1 and UBF2. After incubation for 24 h at 37°C, cells were checked for dotted fluorescence of nucleolar FCs. These cells were briefly rinsed with PBS solution (Gibco, Great Britain), fixed for 10 min in 4% paraformaldehyde (EMS, USA), dissolved in PBS, rinsed repeatedly and processed for LCM and pre-embedding anti-GFP-nanogold immuno-EM.

Preparation of cells for TEM

For conventional TEM, control and treated with AMD cells (either non transfected or transfected), growing in 40 ml boxes as well as seeded on Ø 4 mm glass coverslips were fixed at 60-70% of confluence in 2.5% glutaraldehyde and then post-fixed in 1% OsO_4 (both were EMS) solutions

dissolved in PBS. After fixation cells were washed with deionized water, then detached by scraping off monolayer cultures and harvested in 0.5 ml plastic centrifuge tubes. After sedimentation at 1000 r/pm (5min), deionized water was replaced by 30% BSA. Cells were thoroughly re-suspended and centrifuged repeatedly. The resulting pellet was jellified by adding 2-3 drops of 25% glutaraldehyde during 15-20 min. Finally, the jellified pellet was cut in small cubes in order to get better penetration for dehydrating/impregnating solutions and rinsed again in deionized water. Samples of appropriate size (~1 mm^3) were dehydrated in graded series of acetone and embedded in Embed 812 (EMS) by polymerization in gelatin capsules at 60°C during 48h. About 80-100 nm ultrathin sections were mounted on mesh200 Maxtaform or mesh200 London Finder (both were EMS) copper grids. Before examination, EM sections were counterstained with 5% aqueous solution of uranyl acetate (20-30 min) and lead citrate (3-5 min) then washed thoroughly in deionized water. Images were obtained by means of Hitachi H300 (Hitachi, Japan) EM at 70kV.

Pre-embedding Immuno-EM staining of GFP by fluoronanogold/HQ silver particles

Cells were fixed for 10 min in 4% paraformaldehyde diluted in PBS, then permeabilized with 0.5% Triton X-100 in PBS for 5 min without light (Cheutin et al., 2002; Tchelidze et al., 2008). Cells were soaked for 30 min in 10% normal goat serum (NGS, Jackson, USA) in PBS, then incubated for 30 min with an anti-GFP mouse antibody (Roche Diagnostics) diluted in PBS 1:50. After rising three times in PBS during 5 min, the secondary antibody, which was a biotinylated conjugated affinipure Fab_2 fragment of goat anti-Mouse IgG (Jackson, USA), was applied at 1:100 for 30 min. It was then revealed with a nanogold-Streptavidin conjugate (Nanoprobes, USA) at 1:500 in PBS. After fixation with 1.6% glutaraldehyde in PBS, cells were washed in deionised water and the labeling was amplified with HQ Silver or HQ Gold (both were Nanoprobes) in order to obtain 10 nm particles (Cheutin et al., 2002). To visualize the co-localization between UBTF1-GFP/UBTF2-GFP nucleolar sites and anti-GFP marker, we used the double-label immunofluorescence control. For double labeling, cells after incubation with biotinylated secondary antibodies were exposed for 15 min to streptavidin-Texas Red complex (Amersham Life Science, USA) diluted 1:20.

All procedures for immuno-EM were done at room temperature using light-tight box. The reduced illumination is required to prevent the photoprecipitation of metallic silver during action of silver enhancement reagents (HQSilver Kit, Nanoprobes). After labeling with nanogold streptavidin conjugate, cells were again fixed in 1.6 % glutaraldehyde during 15 min and rinsed 3 times (5 min) in PBS. Before silver enhancer reagents were applied, cells were extensively washed (10x2 min) in deionized water in order to exclude possible precipitation of silver chloride. The silver enhancement was carried out at room temperature (about 20°C) during 7-9 min. Noteworthy that quality of staining is strongly temperature/time-dependent. Therefore, to eliminate background staining the reaction was immediately stopped by rapid immersion of cells in ice-cold deionized water. To complete silver enhancement procedure cells were thoroughly washed again (6x2min) and then exposed for 10 min in 5% aqueous solution of sodium thiosulfate, quenching residual metallic silver. The definitive quality of immunogold-silver labeling was controlled in phase contrast microscope. In properly stained cells the UBF positive nucleolar sites are clearly recognizable as they form dark brown, folded bead-like chains (predominantly in control cells) or relatively big distinct spots (mostly after action of AMD). These sites are in a sharp contrast with pale yellow color of the nucleoplasm.

Samples submitted to immuno-EM and electron tomography were harvested by scraping without post-fixation in OsO_4, then dehydrated and embedded in epoxy resin as described above. Serial ultrathin sections, used for demonstration of label distribution throughout the depth of FC, were stained with uranyl acetate and lead citrate before examination in EM. For electron tomographic study we used 0.5 µm thick sections picked-up exclusively on London Finder copper grids (mesh 200). The properly labeled and positioned cells were selected by checking of placed on the grid sections in the phase contrast microscope.

Fluorescence microscopy

Images of fixed cells were collected using protocol described in our previous work (Cheutin et al, 2002). Preparations selected for LCM were examined and imaged using Bio-Rad MRC-1024ES/Olympus IX70 microscope, using 60x/NA 1.4 plan apochromat objective. The fluorescence of GFP was induced by 488 nm of the excitation beam, using 3-10% of Kr/Ar laser power in combination with VHS and Open filter blocs. Emission light was registered at 515 nm, being obtained by OG515 filter.

In the preparations with double labeling, the fluorescence of Texas Red and DsRed was excited with 543 nm of wavelength while emission light was collected at 620 nm. The fluorescence of GFP and Texas Red as well as GFP and were revealed simultaneously by 488 and 568 nm of the excitation lights, using 10% of the same laser power and T1 and T2 filter blocs. This combination enables simultaneous transmission of both bands and their registration trough green and red channels (PMT2 and PMT1, correspondingly) by means of the following emission filters: first, for green light 522DF35 (blocks the bands of 513 and 540 nm) and second, for red light 605DF32 (blocks waves of 589-621 nm).
Acquisition of Z-stacks (8 bits, 512x512 pixels) was performed by means of Laser Sharp 3.2 software, at zoom x4 that corresponds to one pixel size measured 0.080µm. The slow scanning speed mode (3 sec for each 512x512 image) and Kalman digital filtering (x3) were utilized for the amelioration of signal/noise ratio. Phase contrast and fluorescent images were digitalized simultaneously. Series of consecutive optical sections (ordinarily 70-100 slices) were recorded using 0.2 µm Z-step that yields the stack of ~14-20 µm thick; a room fully including the KB cell nucleus.

3D imaging of UBF1 and UBF2 in fixed control and AMD treated cells was performed with Amira 5.5 software (TGS, Mercury Computer Systems, France) using two methods: (i) the "Isosurface" mode, displaying the exterior morphology (shape, number, and size) by surface rendering and (ii) the "Voltex" mode, representing interior organization by the rendering of the whole volume. Images selected for 2D demonstrations were presented in "Maximum Intensity Projections" (MIP) mode after being processed using regular image-treatment and graphic software such as ImageJ, Corel Draw, and Photoshop etc. (for details see Tchelidze *et al.,* 2006).

Electron tomography and 3D reconstruction

For electron tomography, 500 nm thick sections were investigated, tilted and registered in a STEM CM30 (Philips, The Netherlands) medium-voltage electron microscope working at 250 kV (Heliot *et al.,* 1997; Cheutin *et al.,* 2002; Tchelidze *et al.,* 2008). Before tilting, the grid was properly oriented in EM holder using binoculars (x2), according position of pick on London Finder grid and scheme given in previous work of our group (Tchelidze *et al.,* 2008). Using eucentric goniometer stage each section was tilted every 2° from -60 to +6O°. Corresponding images were directly recorded by photo multiplier detector and then sampled in binary (512x512pxl) format with Orion hardware/software system (ELIsprl, Belgium).
Before 3D reconstruction the contrast of binary images was reversed and they were individually aligned by means of sinogram method (Tchelidze et al., 2006). Tomography reconstruction by tilted series of aligned 512x512pxl images was performed using ART technique. The primarily reconstructed volumes were visualized and extensively investigated in the maximum intensity projection (MIP) mode using the Analyze software (Mayo BIR, CN Software, UK). Selected volumes were submitted to further image restoration treatment, such as deconvolution, filtering etc. (Tchelidze *et al.,* 2008).
Surface and volume visualization, as well as rotation of 3D models around any chosen axis were performed with Amira 5.5 software. The interior organization of the reconstructed volumes was investigated by presenting sections of any chosen plan using "Orthogonal slices" and "Oblique slices" mode. The successive steps of visualization and extraction of sub-volumes from the interior of FC's are imaged on Supplemental figure 7. For each of the UBTF1 and UBTF2 labellings, 12 reconstructions were performed in the KB cells (control: 3, AMD 1h: 5, AMD 3h:4). 9 reconstructions were performed for metaphasic NORs.

Results

1) Fluorescence imaging demonstrates the co-localization of UBTF1 and UBTF2 within control and AMD treated cells.

KB cells were imaged by confocal microscopy (phase contrast and fluorescence) to study their structure before and after transfection (without immunolabeling of GFP or with permeabilization and immunolabeling of GFP) and to study the distribution of UBTF1-GFP and UBTF2-GFP isoforms.

Altogether these studies showed that:

a) control cells contain large nucleoli in which UBTF1-GFP and UBTF2-GFP were found within spheres disposed as so called "necklaces" (Supplemental Figures S1 A-B and G-H);
b) treatment with AMD induced classical segregation of nucleolar components due to the gathering of spheres containing UBTF1-GFP or UBTF2-GFP within the nucleolar territory (AMD treatment for 1 h; Supplemental Figures S1 C-D and I-J) and their shift at the periphery of nucleolus as crescent-like "caps" (AMD treatment for 2 h; Supplemental Figures S1 E-F and K-L);
c) UBTF1 and UBTF2 were co-localized in the same nucleolar structures of doubly transfected cells (UBTF1-GFP and UBTF2-dsRed) without and with AMD treatment (Supplemental Figures S2 A-U).

2) Ultrastructural imaging of UBTF1 and UBTF2 on ultrathin sections of control KB cells demonstrates that they are abundant within FCs but differently distributed.

To precisely localize UBTF1-GFP and UBTF2-GFP within nucleolar components of control and AMD treated cells, we decided to identify GFP antibodies before embedding and to reveal them by using secondary antibodies coupled to nanogold particles. The latter were then enhanced with silver to grow as more visible particles ~10 nm in diameter. Compared to classical post-embedding colloidal gold technique that only identifies molecules present on the surface of ultrathin sections, pre-embedding approach has two decisive advantages. Hence, as we showed using serial ultrathin sections, it allows identification of much more UBTF1-GFP and UBTF2-GFP and it reveals their spatial distribution in the thickness of 80 to 100 nm ultrathin sections (Figure 1 and Supplemental Figures S3, S4, S5 and S6)

By using this approach, we obtained two important results. First, we evidenced that the labeling intensities for UBTF1-GFP or UBTF2-GFP were quite similar within a given nucleolar sub-compartment but strongly varied from one sub-compartment to another one. Thus, labeling intensities were (Figure 1 and Supplemental Figures S3 and S5): i) very low within DFC and GC, ii) low within nucleolar interstices and nucleoplasm and iii) very high within FCs. Second, we revealed that the distribution of UBTF1-GFP molecules within FCs was different to that of UBTF2-GFP molecules (compare Figure 1A and D).

Within small and large FCs (i.e. around 0.5 µm and 0.9 – 1.2 µm in diameter respectively), UBTF1-GFP was not localized at random but was distributed into several clusters whose diameter ranged from 60 to 100 nm (Figure 1A and Supplemental Figures S3). In small FCs, these clusters frequently appeared as parts of linear or curved coils (200 and 300 nm long respectively). Noteworthy, these clusters were reminiscent of transversal and longitudinal sections of Pol I-positive coils 60 nm in diameter and 200 nm in length we previously described within FCs (Cheutin et al., 2002). We also note that UBTF1-GFP localized in the nucleoplasm was either dispersed or grouped in small clusters within condensed chromatin (Supplemental Figures S3).

In contrast, UBTF2-GFP was not distributed in clusters but was evenly dispersed within FCs (Figure 1B and Supplemental Figures S5). Within smaller FCs (Figure 1B), UBTF2-GFP was homogeneously dispersed. Interestingly, within largest FCs (0.9 to 1.2 µm), UBTF2-GFP was preferentially localized within the cortical part of FCs (0.4 µm in thickness) but was absent in their central region (around 0.4 µm in diameter) (Supplemental Figures S5 H). We also note that UBTF2-GFP molecules localized in the nucleoplasm were evenly dispersed and not grouped as small clusters (Supplemental Figures S5 A-H).

3) Ultrastructural localization of UBTF1 and UBTF2 on ultrathin sections of KB cells treated with AMD for 1h demonstrates they are in part similarly distributed within gathering fibrillar centers.

By using the same approach as in control cells, we showed that the labeling intensities for UBTF1-GFP or UBTF2-GFP in cells treated with AMD for 1h remained quite similar within a given nuclear compartment but strongly varied from one compartment to another one. Thus, labeling intensities were: i) very low within nucleolar interstices and within reorganized DFC and GC, ii) low within nucleoplasm and iii) very high within gathering FCs (Figure 1B and E and Supplemental Figures S4 and S6). Moreover, we revealed that the distribution of UBTF1-GFP and UBTF2-GFP within gathering FCs changed relatively to control cells and became quite identical when the duration of treatment with AMD increased.

After 1 h of treatment with AMD, UBTF1-GFP were partly grouped as several 60 to 100 nm clusters, constituting elongated linear and/or curved coils that were less compact than in control cells, frequently giving rise to rows of single particles disposed as loop-like structures (Figure 1B and Supplemental Figures S4 A-F). Concerning UBTF2-GFP, one part was dispersed as in control cells and another part was aligned giving rise to rows of single particles disposed as loop-like structures (Figure 1E and Supplemental Figures S6 A-E).

4) Ultrastructural localization of UBTF1 and UBTF2 on ultrathin sections of cells treated with AMD for 2h demonstrates that they are similarly distributed within caps.

After 2 h of treatment with AMD, nucleoli were fully segregated. Labeling intensities for UBTF1-GFP or UBTF2-GFP molecules were similar within a given nuclear compartment. They were very low within nucleoplasm and segregated dense fibrillar and granular components but very high within FCs gathered as crescent-like nucleolar caps (Figure 1C and F). Interestingly, UBTF1-GFP and UBTF2-GFP were similarly disposed within nucleolar caps. Thus, particles identifying UBTF1-GFP and UBTF2-GFP were no more grouped into clusters or completely dispersed but appeared as single particles mostly linearly disposed into curved or looped filaments or fibers (Figure 1C and F and Supplemental Figures S4 G-I and S6 F-G). In nucleoplasm and condensed chromatin, UBTF1-GFP and UBTF2-GFP were not grouped but completely dispersed.

5) Electron tomography of UBTF1 and UBTF2 demonstrates that their 3D distribution is different in control cells but similar in AMD treated cells.

Considering that imaging of particles contained within 80-100 nm ultrathin sections was not sufficient to definitely conclude on the spatial distribution of UBTF1-GFP and UBTF2-GFP, we decided to address that point by using electron tomography. Thus, the labeling was imaged within 500 nm thick sections by using a Scanning Transmission Electron Microscope (STEM) working at 250kV (Cheutin *et al.*, 2002; Tchelidze *et al.*, 2008). Thick sections were tilted every 2° from -60° to + 60° and the images were perfectly aligned and used to perform tomographic reconstructions (Tchelidze *et al*., 2006). The whole reconstructions and chosen sub-volumes were then rotated in different directions. Virtual slices and 3D visualization were performed to determine whether particles localizing UBTF1-GFP and UBTF2-GFP were disposed at random or were disposed as more or less complex 3D structures such as looped fibrils or coils (Supplemental Figures S7 A-L).

In thick sections of nucleoli of control cells, particles identifying UBTF1-GFP or UBTF2-GFP were extremely numerous and grouped as spheroid clusters 300 to 500 nm in diameter that corresponded to FCs. In clusters of UBTF1-GFP, particles were either grouped as coils or frequently aligned as contorted loops (Figure 2 A-K). In contrast, in clusters of UBTF2-GFP molecules, only some particles were organized as fibers and contorted loops whereas numerous particles were randomly disposed within the cortical part of FCs (Figure 3 A-J).

AMD treatment for 1 h induced the step by step gathering of several initial FCs and gave rise to enlarged FCs. In the latter, particles identifying UBTF1-GFP or UBTF2-GFP were grouped as large and irregular clusters 600 to 850 nm in size. 3D imaging evidenced that these large clusters were lobulated due to the gathering of unfused FCs (Figure 4 A-C and Supplemental Figure S8 A-C). Interestingly,

virtual sections and 3D visualization of sub-volumes performed in tomograms clearly evidenced that particles identifying UBTF1-GFP (Figure 4 D-K) or UBTF2-GFP (Supplemental Figure S8 D-L) were similarly organized in 3D i.e. were aligned as long twisted and contorted loops.

AMD treatment for 2 h induced a more complete gathering of FCs that constitute crescent-shaped structures (or caps) up to 2 µm long located on the outer part of nucleolar remnants. Particles identifying UBTF1-GFP or UBTF2-GFP were not homogeneously distributed but grouped as several globular structures disposed close together (Figure 5 A-B and I). Virtual sections and 3D visualization of sub-volumes performed in tomograms of caps clearly evidenced that particles identifying UBTF1-GFP (Figure 5 C-H) or UBTF2-GFP (Figure 5 I-L) were similarly distributed as long twisted and contorted loops. It is also interesting to note that identical results were observed in A549 cells (Supplemental Figures S9-11).

6) Electron tomography of UBTF1 and UBTF2 demonstrates that their 3D distribution in metaphase NORs is similar to that of nucleolar caps in AMD treated cells.

As UBTF1-GFP and UBTF2-GFP molecules were similarly redistributed as long twisted loops due to rRNA inhibition induced by AMD, we asked whether natural inhibition of rRNA synthesis during mitosis could induce a different spatial reorganization.

In a first step, KB cells were doubly transfected with histone H2B-GFP and UBTF1 or UBTF2-DsRed and were imaged by confocal microscopy to confirm that UBTF1 and UBTF2 were located in metaphase NORs (Figure 6 A). As earlier described (Klein et al., 1998), the latter appeared as small, medium or large spherical or ellipsoid structures. Then, the 3D disposition of UBTF1-GFP or UBTF2-GFP molecules was studied by electron tomography as above (Figure 6 B-I and Figure 7 A-K). This study showed that, in all types of metaphase NORs, the 3D organization of UBTF1-GFP molecules was strictly similar to that of UBTF2-GFP molecules. On Figure 6 B-I two medium-sized metaphase NORs were imaged in a cell transfected with UBTF1-GFP plasmid. 3D surface visualization and virtual slicing at high magnification showed that particles identifying UBTF1-GFP were disposed as folded and twisted loop-like fibrils as we previously found in AMD treated cells. The same 3D distribution was found in metaphase cells synthetizing UBTF2-GFP (Figure 7 A-K).

Discussion:

In order to reveal the role played by the two variants of UBTF, we examined in great detail their localization in cells where the transcription of ribosome genes is active and inhibited naturally (mitosis entry) or artificially (AMD treatment).

During interphase, we here demonstrated that UBTF1 and UBTF2 were not present in DFC and GC but, in contrast, were very abundant within FCs of KB cells which are now identified as HeLa cells (Vaughan *et al.*, 2017). By using a cryo-nano-analytical approach, we previously demonstrated that FCs are the most hydrated sub volumes in the nucleus of HeLa cells (Nolin *et al.*, 2013). More precisely, we recently quantified that 80% and 20 % of the volume of FCs are occupied with free water and hydrated macromolecules respectively (Michel *et al.* 2019). We also evidenced that DFC and GC are less hydrated and are more compact than FCs because 60 % and 40 % of their volume are occupied with free water and hydrated macromolecules respectively (Michel *et al.* 2019).

Considering that rRNA genes are contained within FCs (Thiry *et al.,* 1991; Puvion *et al.,* 1992; Derenzini *et al.,* 1993; Thiry and Goessens, 1996; Derenzini *et al.,* 2006) and that UBTF is only associated to enhancer, transcribed region and spacer terminator of rDNA (Hamdane *et al.,* 2014; Herdman *et al*, 2017; Moss *et al*, 2019), we propose that the different levels of interaction of UBTF1 and UBTF2 with rDNA might modulate their distribution within FCs. Thus, the inactivity of UBTF2 in Pol I transcription (O'Mahony *et al.,* 1991; Kuhn *et al.,* 1994; Cavanaugh *et al.,* 2003) and its low capacity to remodel r-chromatin (Sanij *et al.,* 2008) might result in its random location within FCs. In contrast, the recently recognized role of UBTF1 as a main regulator of Pol I (Sanij *et al.*, 2015) and in maintaining rRNA genes in an open configuration (Sanij *et al.,* 2008; McStay 2016; Herdman et al, 2017; Moss et al, 2019) might explain its distribution along fibers that we propose to use to trace r-chromatin within FCs.

The 3D organization of UBTF1 as coils 200 to 300 nm in length and 60 to 100 nm in diameter and along looped fibers we described in the present paper is reminiscent of that of Pol I molecules we previously described in a three-dimensional model of rDNA (Cheutin *et al.,* 2002). However, we found that the 3D organization of UBTF1 was less obvious than that of Pol I. This characteristic could come from a slightly different distribution of UBTF1 and Pol I molecules along the 47S transcribed region of the rDNA as recently revealed by the use of a new deconvolution protocol for ChIP-Seq (Herdman et al, 2017; Mars et al., 2018). These studies revealed that the distribution of UBF was not uniform and "form a semicontinuous pseudochromatin across the transcribed region of the rDNA" whereas the distribution of Pol I molecules along the transcribed ribosomal gene body was very uniform (Mars et al., 2018). These analyses also revealed an Enhancer Boundary Complex formed by the transcriptional repressor CTCF and the chromosome-associated multisubunit protein complex cohesin that delimit each functional rRNA gene and stabilize their looping (Herdman et al, 2017). To note, this finding is coherent with the organization of one rDNA gene as a complex loop based on the gathering of the two flanking IGS as suggested by their ultrastructural location in interstices in close contact with FCs (Thiry and Thiry-Blaise, 1991).

Here, we propose to improve this model by integrating the finding that promoter, upstream region and terminator R3 of rDNA constitute a central core within FC (Denissov *et al.,* 2011). This new model is presented in Figure 8 and Supplemental movie 1. In this model, one spread rDNA repeat is first drawn at scale on Figure 8A. It shows (from left to right) one IGS in red, one enhancer in purple, one transcribed unit with 100 associated Pol I molecules, one terminator in blue and next IGS in red. On next views (Figure 8B-Q) we propose successive steps needed to wrap this spread rDNA in 3D in order to finally position it within one FC with the constraint of maintaining its uncondensed state. In a first step, the two IGS flanking the transcribed unit are condensed (Figure 8B, C) and gathered (Figure 8D, E). Enhancer and terminator are maintained as uncondensed loops that are grouped as a central core around which the transcribed region constitutes four extended loops (Figure 8E). In the next steps, (Figure 8F-K), these 4 loops strongly fold to constitute 4 separate shorter coils that bend around enhancer and terminator loops (Figure 8K). Finally, (Figure 8L-N), growing pre-rRNA molecules are drawn as green threads ended with a terminal knob at their 5' end (Trendelenburg *et al.,* 1996) that directly enter surrounding DFC (transparent green curved tubes) (Puvion-Dutilleul *et al.,* 1991, 1997).

This model agrees with the distribution of UBTF1 and UBTF2 we demonstrated in the present paper. Thus:

a) the association of UBTF to enhancer, transcribed region and spacer terminator of rDNA (Hamdane *et al.,* 2014; Herdman *et al*, 2017; Moss *et al*, 2019), fits to a slightly different distribution of UBTF1 molecules and of Pol I i.e. along coils and loops,
b) the weak (or absence of) interaction of UBTF2 molecules with r-chromatin in control cells (Sanij *et al.*, 2008) induces their homogeneous distribution in the cortical volume of FCs.

In summary, our model proposes that an active rRNA gene occurs in a multi-folded looped organization occupying a globular structure, or *r-Chromatin Globule* (r-CG), which is strongly reminiscent of the recently described *Chromatin Extrusion Globules* (Sanborn et al., 2015). Each r-CG can form single FC in nucleolus of control cells or can be gathered into larger FCs or caps due to inactivation.

Thus, each FC appears as a highly hydrated volume (Michel *et al.*, 2019) that gathers uncondensed rDNA and high concentration of specific factors (Pol I, UBTF etc.). We suggest that all these conditions might be necessary to ensure the high elongation rate of rRNA (Dundr *et al.,* 2002).

Our model also places the 3' and 5' extremities of growing rRNA in two different compartments. The first one is cortex of FC where rRNAs are elongated by Pol I and the second one is DFC that is an anchorage site for U3 snRNP (Puvion-Dutilleul *et al.,* 1992) in which rRNA processing is initiated. As hydrated macromolecules occupy 20% and 40 % of the volume of FCs and DFC respectively (Michel *et al.*, 2019) growing rRNAs have to cross a phase boundary in order to reach DFC whose higher molecular crowding might correlate with its high viscoelastic properties (Feric *et al.,* 2016). This might induce a liquid-liquid phase separation that is a characteristic of cell compartments (Banani *et al.,* 2017) and

more particularly those in which transcription takes place (Hniisz *et al.,* 2017) such as the nucleolus (Mitrea and Kriwack, 2016; Falahati and Wieschaus, 2017; Mangan *et al.,* 2017).

Our study also demonstrated that the different changes observed within caps induced by AMD were similar to that of mitotic NORs. First, we showed that both caps induced by AMD and mitotic NORs were constituted by several globular structures suggesting the gathering but not the fusion of several FCs. This might result from concomitant contraction of nucleolar condensed chromatin (Tchelidze *et al.,* 2017) and gathering of FCs that contain uncondensed rDNA (Puvion-Dutilleul *et al.,* 1992) during AMD treatment. Such reorganization is reminiscent of the one that takes place during prophase and prometaphase (Ploton *et al.,* 1987). Second, we showed that UBTF1 and UBTF2 were simultaneously present during AMD treatment and during mitosis but that their localization and 3D distribution were strongly modified relatively to control cells. Such modifications could be induced by the competition of AMD against UBTF for enhancer binding (Copenhaver *et al.,* 1994) and inactivation of UBTF by its phosphorylation in mitotic NORs (Klein and Grummt, 1999). However, such molecular modifications do not freeze UBTF1 and 2 on rDNA. In contrast, within caps (Shav-Tal *et al.,* 2005) and within mitotic NORs (Chen et al., 2005), UBTF1 and 2 maintain a high dynamic as they have during interphase (Dundr *et al.,* 2002).

The comparison of UBTF1 and UBTF2 localization in control and inactive cells (AMD treated and mitotic NORs), allowed us to propose that active rDNA might be associated only with UBTF1 whereas inactive rDNA might be associated with both UBTF1 and UBTF2. This is in agreement with the hypothesis (Sanij *et al.,* 2008) that replacing UBTF1 homodimers with UBTF1 and 2 heterodimers or UBTF2 homodimers might decrease the number of active rRNA genes. Considering that UBTF1 traces the 3D localization of rDNA (see model on Figure 8), our study suggests the existence of two different 3D organization of uncondensed rDNA. The first one concerns active rDNA that is constituted of small loops that are bent by UBTF1 molecules (Kuhn *et al.,* 1994) to organize long coils in FCs. The second one concerns inactive rDNA, which is no longer organized as coils, but as more extended twisted loops associated with UBTF1 and UBTF2 in nucleolar caps and mitotic NORs. The hypothesis that nucleolar caps contain very uncondensed rDNA agrees with our finding that 90 % and 10 % of their volume are occupied with free water and hydrated macromolecules respectively (Michel *et al.*, 2019). In comparison, hydrated macromolecules occupy up to 50 % of the volume of condensed interphase and mitotic chromatin (Michel *et al.*, 2019). It is known that metaphase NORs are rapidly reactivated at the end of mitosis due to their bookmark with UBTF (Roussel *et al.,* 1993; Gebrane *et al.* 1997; Klein *et al.,* 1998; Grob et *al.,* 2014; Mc Stay, 2016). Our present study now demonstrated that mitotic NORs are very likely bookmarked by the presence of both UBTF1 and 2 molecules associated to highly under condensed rDNA (Heliot *et al.,* 1997).

In conclusion, we demonstrated that UBTF1 and UBTF2 were simultaneously localized in the same sub-compartments containing either active rDNA (in FCs) or inactive rDNA (in nucleolar caps and mitotic NORs). Electron tomography evidenced that UBTF1 was distributed along loops of active and inactive rDNA whereas UBTF2 was localized at random around the loops of active rDNA and was associated to extended 3D loops of inactive rDNA. These data suggest new roles for UBTF1 and 2 isoforms that specifies their roles in highly transcribed genes (Hamdane et *al.,* 2015).

Acknowledgments:
We acknowledge:

- the Platform of Cellular and Tissular Imaging (PICT) of URCA University, Reims, France for the availability of equipment,

- Dr. Marie-France O'Donohue for the construction of fusion proteins,

- Nicolas Ploton for 3D modelling of rDNA globule.

References:

Andersen, J.S., Lam, Y.W., Leung, A.K.L., Ong, S.E., Lyon, C.E., Lamond A., Mann, M., 2005. Nucleolar proteome dynamics. Nature 433, 77-83.

Andersen, J.S., Lyon, C.E., Fox, A.H., Leung, A.K.L., Lam, Y.W., Steen, H., Mann, M., Lamond, A., 2002. Directed proteomic analysis of the human nucleolus. Curr. Biol. 12, 1-11.

Banani, S.F., Lee, H.O., Hyman, A.A., Rosen, M.K. 2017. Biomolecular condensates: organizers of cellular biochemistry. Nature Rev. Mol. Cell. Biol. 18, 285-298.

Cavanaugh, A., Hirchler-Laszkiewicz, I., Rothblum, L., 2003. Ribosomal DNA transcription in mammals. In: The Nucleolus, ed. M.O. Olson, Plenum Publisher, pp. 89-129.

Chen, D., Dundr, M., Wang, C., Leung, A., Lamond, A., Misteli, T., Huang, S., 2005. Condensed mitotic chromatin is accessible to transcription factors and chromatin structural proteins. J. Cell Biol. 168, 41-54.

Cheutin, T., O'Donohue, M.-F., Beorchia, A., Vandelaer, M., Kaplan, H., Defever, B., Ploton, D., Thiry, M., 2002. Three-dimensional organization of active rRNA genes within the nucleolus. J. Cell Sci. 115, 3297-3307.

Copenhaver, G.P., Putnam, C.D., Denton, M.L., Pikaard, C.S., 1994. The RNA polymerase I transcription factor UBF is a sequence-tolerant HMG-box protein that can recognize structured nucleic acids. Nucleic Acids Res. 22, 2651-2657.

Denissov, S., Lessard, F., Mayer, C., Stefanovsky, V., Van Driel, M., Grummt, I., Moss, T., Stunnenberg, H.G., 2011. A model for the topology of active ribosomal RNA genes. EMBO reports 12, 231-237.

Derenzini, M., Pasquinelli, G., O'Donohue, M.-F., Ploton, D., Thiry, M., 2006. Structural and functional organization of ribosomal genes within the mammalian cell nucleolus. J. Histochem. Cytochem. 54, 131-145.

Derenzini, M., Farabegoli, F., Trere, D., 1993. Localization of DNA in the fibrillar components of the nucleolus: a cytochemical and morphological study. J. Histochem. Cytochem. 41, 829-836.

Dundr, M., Hoffmann-Rohrer, U., Hu, Q., Grummt, I., Rothblum, L.I., Phair, R.D., Misteli, T., 2002. A kinetic framework for a mammalian RNA polymerase in vivo. Science 298, 1623-1626.

Falahati, H., Wieschaus, E., 2017. Independent active and thermodynamic processes govern the nucleolus assembly in vivo. Proc. Natl. Acad. Sci. USA 114, 1335-1340.

Farley, K.I., Surovtseva, Y., Merkel, J., Baserga, S.J., 2015. Determinants of mammalian nucleolar architecture. Chromosoma 124, 323-331.

Feric, M., Vaidya, N., Harmon, T.S., Mitrea, D.M., Zhu, L., Richardson, T.M., Kriwacki, R.W., Pappu, R.V., Brangwynne, C.P., 2016. Coexisting liquid phases underlie nucleolar subcompartments. Cell 165, 1-12.

Gebrane-Younes, J., Fomproix, N., Hernandez-Verdun, D., 1997. When rDNA transcription is arrested during mitosis, UBF is still associated with non-condensed rDNA. J. Cell Sci. 110, 2429-2440.

Goodfellow, S.J., Zomerdjik, J.C.B.M., 2012. Basic mechanisms in RNA polymerase I transcription of the ribosomal RNA genes. Subcell. Biochem. 61, 211-236.

Grob, A., Colleran, C., McStay, B., 2014. Construction of synthetic nucleoli in human cells reveals how a major functional nuclear domain is formed and propagated through cell division. Genes Dev. 28, 220-230.

Grummt, I., 2003. Life on a planet of its own: Regulation of RNA polymerase I transcription in the nucleolus. Genes Dev. 17, 1691-1702.

Hamdane, N., Stefanovsky, V.Y., Tremblay, M.G., Németh, A., Paquet, E., Lessard, F., Sanij, E., Hannan, R., Moss, T., 2014. Conditional inactivation of upstream binding factor reveals its epigenetic functions and the existence of a somatic nucleolar precursor body. PLOS Genet. 10, e1004505.

Heliot, L., Kaplan, H., Lucas, L., Klein, C., Beorchia, A., Doco-Fenzy, M., Menager, M., Thiry, M., O'Donohue, M.-F., Ploton, D., 1997. Electron tomography of metaphase nucleolar organizers regions: evidence for a twisted-loop organization. Mol. Biol. Cell 8, 2199-2216.

Henras, A.K., Plisson-Chastang, C., O'Donohue, M.-F., Chakraborty, A., Gleizes, P.E., 2015. An overview of pre-ribosomal RNA processing in eukaryotes. WIRES RNA 6, 225- 242.

Herdman, C., Mars, J.C., Stefanovsky, V.Y., Tremblay, M.G., Sabourin-Felix, M., Lindsay, H., Robinson, M.D., Moss, T., 2017. A unique enhancer boundary complex on the mouse ribosomal RNA genes persists after loss of Rrn3 or UBF and the inactivation of RNA polymerase I transcription. PLoS Genet. 13, e1006899.

Hernandez-Verdun, D., Roussel, P., Thiry, M., Sirri, V., Lafontaine, D., 2010. The nucleolus: structure/function relationship in RNA metabolism. WIRES RNA 1, 415-431.

Hnisz, D., Shrinivas, K., Young, R.A., Chakraborty, A.K., Sharp, P.A., 2017. A phase separation model for transcriptional control. Cell 169, 13-23.

Klein, C., Cheutin, T., O'Donohue, M.-F., Rothblum, L.I., Kaplan, H., Beorchia, A., Lucas, L., Heliot, L., Ploton, D., 1998. The three-dimensional study of chromosomes and of UBF-immunolabeled NOR's demonstrates their non-random spatial arrangement during mitosis. Mol. Biol. Cell 9, 3147-3159.

Klein, J., Grummt, I., 1999. Cell cycle-dependant regulation of RNA polymerase I transcription: the nucleolar transcription factor UBF is inactive in mitosis and early G1. Proc. Natl. Acad. Sci. USA 96, 6096-6101.

Koberna, K., Malinski, J., Pliss, A., Masata, M., Vecerova, M., Fialova, M., Bednar, J., Raska, I., 2002. Ribosomal genes in focus: new transcripts label the dense fibrillar components and form clusters indicative of "Christmas trees" in situ. J. Cell Biol. 157, 743-748.

Krüger, T., Zentgraf, H., Scheer, U., 2007. Intranucleolar sites of ribosome biogenesis defined by the localization of early binding ribosomal proteins. J. Cell Biol. 177, 573-578.

Kuhn, A., Voit, R., Stefanovsky, V., Evers, R., Bianchi, M., Grummt, I., 1994. Functional difference between the two splice variants of the nucleolar transcription factor UBF: the second HMG box determines specifity of DNA binding and transcriptional activity. EMBO J. 13, 416-424.

Lamaye, F., Galliot, S., Alibardi, L., Lafontaine, D.L., Thiry, M., 2011. Nucleolar structure across evolution: the transition between bi- and tri-compartmentalized nucleoli lies within the class Reptilia. J. Struct. Biol. 174, 352-359.

Mais, C., Wright, J.E., Prieto, J.L., Raggett, S.L., McStay, B. 2005. UBF-binding site arrays form pseudo-NORs and sequester the RNA polymerase I transcription machinery. Genes Dev. 19, 1-15.

Mangan, H., Gailin, M.O., Mcstay, B., 2017. Integrating the genomic architecture of human nucleolar organizer regions with the biophysical properties of nucleoli. FEBS J 284, 3977-3985.

McStay, B., 2016. Nucleolar organizer regions: genomic 'dark matter' requiring illumination. Genes Dev. 30, 1598-610.

Mars, J.C., Sabourin-Felix, M., Tremblay, M.G., Moss, T., 2018. A Deconvolution Protocol for ChIP-Seq Reveals Analogous Enhancer Structures on the Mouse and Human Ribosomal RNA Genes. G3 (Bethesda) 8, 303-314.

Michel, J., Nolin, F., Wortham, L., Lalun, N., Tchelidze, P., Banchet, V., Terryn, C., Ploton, D., 2019. Various nucleolar stress inducers result in highly distinct changes in water, dry mass and elemental content in cancerous cell compartments: investigation using a nano-analytical approach. Nanotheranostics 3, 179-195.

Mitrea, D.M., Kriwack, R.W. 2016. Phase separation in biology; functional organization of a higher order. Cell comm. Signal. 14, 1-20.

Moss, T., 2004. At the crossroads of growth control ; making ribosomal RNA. Curr. Opi. Genet. Dev. 14, 1-8.

Moss, T., Mars, J.C., Tremblay, M.G., Sabourin-Felix, M., 2019. The chromatin landscape of the ribosomal RNA genes in mouse and human. Chromosome Res. 27, 31-40.

Nicolas, E., Parisot, P., Pinto-Monteiro, C., de Walque, R., de Vleeschouwer, C., Lafontaine, D.L.J. 2016. Involvement of human ribosomal proteins in nucleolar structure and p53-dependent nucleolar stress. Nat comm. 7, 11390.

Nolin, F., Michel, J., Wortham, L., Tchelidze, P., Balossier, G., Banchet, V., Bobichon, H., Lalun, N., Terryn, C., Ploton, D., 2013. Changes to cellular water and element content induced by nucleolar stress: investigation by a cryo- correlative nano imaging approach. Cell. Mol. Life Sci. 70, 2383- 2394.

O'Mahony, D.J., Rothblum, L.I. 1991a. Identification of two forms of the RNA polymerase I transcription factor UBF. Proc. Natl. Acad. Sci. USA 88, 3180-3184.

O'Mahony, D.J., Smith, S.D., Xie, W., Rothblum, L.I., 1991b. Analysis of the phosphorylation, DNA-binding and dimerization properties of the RNA polymerase I transcription factors UBF1 and UBF2. Nucleic acids research 20, 1301-1308.

Ploton, D., Thiry, M., Ménager, M., Lepoint, A., Adnet, J.J., Goessens, G. 1987. Behaviour of nucleolus during mitosis. A comparative ultrastructural study of various cancerous cell lines using the Ag-NOR staining procedure. Chromosoma 95, 95-107.

Puvion-Dutilleul, F., Puvion, E., Bachellerie, J.-P. 1997. Early stages of pre-rRNA formation within the nucleolar ultrastructure of mouse cells studied by in situ hybridization with a 5'ETS leader probe. Chromosoma 105, 496-505.

Puvion-Dutilleul, F., Mazan, S., Nicoloso, M., Pichard, E., Bachellerie, J.-P., Puvion, E., 1992. Alterations of nucleolar ultrastructure and ribosome biogenesis by actinomycin D. Implications for U3 snRNP function. Eur. J. Cell Biol. 58, 149-162.

Puvion-Dutilleul, F., Bachellerie, J.-P., Puvion, E., 1991. Nucleolar organization of HeLa cells as studied by in situ hybridization. Chromosoma 100, 395-409.

Raska I, Koberna K, Malínský J, Fidlerová H, Masata M., 2004. The nucleolus and transcription of ribosomal genes. Biol. Cell. 96, 579-594.

Roussel, P., Andre, C., Masson, C., Geraud, G., Hernandez-Verdun, D., 1993. Localization of the RNA polymerase I transcription factor hUBF during the cell cycle. J. Cell Sci. 104, 327-337.

Sanborn, A., Rao, S., Huang, S.C., Durand, N., Huntley, M., Jewett, A., Bochkov, I., Chinnappan, D., Cutkosky, A., Li, J., Geeting, K., Gnirke, A., Melnikov, A., McKenna, D., Stamenova, E., Lander, E., Aiden, E., 2015. Chromatin extrusion explains key features of loop and domain formation in wild-type end engineered genomes. Proc. Natl. Acad. Sci. USA 10, 1-41.

Sanij, E., Diesch, J., Lesmana, A., Poortinga, G., Hein, N., Lidgerwood, G., Cameron, D.P., Ellul, J., Goodall, G.J., Wong, L.H., Dhillon, A.S., Hamdane, N., Rothblum, L.I., Pearson, R.B., Haviv, I., Moss, T., Hannan R.D., 2015. A novel role for the Pol I transcription factor UBTF in maintaining genome stability through the regulation of highly transcribed Pol II genes. Genome Res. 25, 201-212.

Sanij, E., Poortinga, G., Sharkey, K., Hung, S., Holloway, T.P., Quin, J., Robb, E., Wong, L.H., Thomas, W.G., Stefanovsky, V., Moss, T., Rothblum, L., Hannan, K.M., McArthur, G.A., Pearson, R.B., Hannan, R.D., 2008. UBF levels determine the number of active ribosomal RNA genes in mammals. J. Cell Biol. 183, 1259-1274.

Scheer, U., Hock, R., 1999. Structure and function of the nucleolus. Curr. Opin. Cell Biol. 11,385-390.

Shav-Tal, Y., Blechman, J., Darzacq, X., Montagna, C., Dye, B.T., Patton, J.G., Singer, R.H., Zipori, D., 2005. Dynamic sorting of nuclear components into distinct nucleolar caps during transcriptional inhibition. Mol. Biol. Cell 16, 2395-2413.

Stefanovsky, V., Langlois, F., Gagnon-Kugler, T., Rothblum, L.I., Moss, T., 2006. Growth factor signaling regulates elongation of RNA polymerase I transcription in mammals via UBF phosphorylation and r-chromatin remodeling. Mol. Cell 21, 629-639.

Tafforeau, L., Zorbas, C., Langhendries, J.L., Mullineux, S.T., Stamatopoulou, V., Mullier, R., Wacheul, L., Lafontaine, D.L.J. 2013. The complexity of human ribosome biogenesis revealed by systematic nucleolar screening of pre-rRNA processing factors. Mol. Cell 51, 539-551.

Tchelidze, P., Benassarou, A., Kaplan, H., O'Donohue, M.-F., Lucas, L., Terryn, C., Rusishvili, L., Mosidze, G., Lalun, N., Ploton, D., 2017. Nucleolar sub-compartments in motion during rRNA synthesis inhibition: Contraction of nucleolar condensed chromatin and gathering of fibrillar centers are concomitant. PLoS One 12, e0187977.

Tchelidze, P., Kaplan, H., Beorchia, A., O'Donohue, M.O., Bobichon, H., Lalun, N., Wortham, L., Ploton, D., 2008. Three-dimensional reconstruction of nucleolar components by electron microscope tomography. Hancock, R., ed. The Nucleus : vol 1 : Humana Press

Tchelidze, P., Sauvage, C., Bonnet, N., Kilian, L., Beorchia, A., O'Donohue, M.-F., Ploton, D., Kaplan, H., 2006. Electron tomography of amplified nanogold immunolabelling: Improvement of quality based on alignment of projections with sinograms and use of post-reconstruction deconvolution. J. Struct. Biol. 156, 421-431.

Thiry, M., Lafontaine, D., 2005. Birth of a nucleolus: the evolution of nucleolar compartments. Trends Cell Biol. 15, 194-199.

Thiry, M., Cheutin, T., O'Donohue, M.-F., Kaplan, H., Ploton, D., 2000. Dynamics and three-dimensional localization of ribosomal RNA within the nucleolus. RNA 6, 1750-1761.

Thiry, M., Goessens, G., 1996. The nucleolus during the cell cycle. In: Molecular Biology Intelligence Unit, ed. R.G. Landes Company, Springer-Verlag, Heidelberg, Germany.

Thiry, M., Scheer, U., Goessens, G., 1991a. Localization of nucleolar chromatin by immunocytochemistry and in situ hybridization at the electron microscopic level. Electr. Microsc. Rev. 4, 85-110.

Thiry, M., Thiry-Blaise, L., 1991b. Locating transcribed and non-transcribed rDNA spacer sequences within the nucleolus by in situ hybridization and immunoelectron microscopy. Nucleic Acids Res. 19, 11-15.

Trendelenburg, M.F., Zatsepina, O.V., Waschek, T., Schlegel, W., Tröster, H., Rudolph, D., Schmahl, G., Spring, H., 1996. Multiparameter microscopic analysis of nucleolar structure and ribosomal gene transcription. Histochem. Cell Biol. 106, 167-192.

Vaughan, L., Glänzel, W., Korch, C., Capes-Davis, A., 2017. Widespread Use of Misidentified Cell Line KB (HeLa): Incorrect Attribution and Its Impact Revealed through Mining the Scientific Literature. Cancer Res. 77, 2784-2788.

Zatsepina, O.V., Voit, R., Grummt, I., Spring, H., Semenov, M., Trendelenburg, M.F., 1993. The RNA polymerase I specific transcription factor UBF is associated with transcriptionally active and inactive ribosomal genes. Chromosoma 102, 599-611.

Zimmerman, S.B., Minton, A.P., 1993. Macromolecular crowding: biochemical, biophysical and physiological consequences. Annu. Rev. Biophys. Struct. 22, 27-65.

Figure Legends

FIGURE 1: Electron microscopy reveals different distribution of UBTF1-GFP and UBTF2-GFP in FCs and caps. (A-C) Ultrastructural distribution of UBTF1-GFP in (A) control, (B) pre-segregated (AMD treatment for 1h) and (C) segregated nucleoli (AMD treatment for 2h). In (A) control cells, particles localizing UBTF1-GFP are only present within FC (dotted lines) and are distributed as curved coils 60 to 100 nm in diameter and 200-300 nm long (arrows). In contrast, in pre-segregated and segregated nucleoli, particles localizing UBTF1-GFP are mainly distributed as single rows (arrows on B and C). Particles are rarely detected in DFC regions (a DFC cap is limited with a dotted line on C). (D-F) Ultrastructural distribution of UBTF2-GFP in (D) control, (E) pre-segregated (AMD treatment for 1h) and (F) segregated

nucleoli (AMD treatment for 2h). In (D) control cells, particles localizing UBTF2-GFP are only present within FC (dotted lines) and, in contrast to UBTF1-GFP, are distributed at random. Interestingly, in (E) pre-segregated and (F) segregated nucleoli, UBTF2-GFP are distributed as single rows (arrows) similarly to UBTF1-GFP. chr: chromatin; dfc: dense fibrillar component; NV: nucleolar vacuoles (interstices). Scale bars, 500 nm.

FIGURE 2: Electron tomography reveals the distribution of UBTF1-GFP as coils and loops in FCs of control cells. (A-C) 3D visualization and rotation of one tomogram evidenced that particles were distributed along fibrils that are organized as coils and loops. (D-G) 100 nm thick sub-volumes were cut from the tomogram and maximum intensity projection (MIP mode) was performed in different directions to evidence fibrils. The loop like folding of fibrils is clearly visible in all directions: we marked some of them with dotted lines in F and G. (H-K) Parts of fibrils isolated from the interior of the coil were visualized at higher magnification in 3D and rotated to evidence their folding and bending. Scale bars, 500 nm.

FIGURE 3: Electron tomography reveals the distribution of UBTF2-GFP at random in FC of control cells. (A-C) 3D visualization and rotation of one tomogram at low magnification evidenced that particles were very abundant in the cortical part of the FC and were rare in its central part. Only some particles were organized as fibers and contorted loops. (D-G) Successive projections of virtual sub-volumes (~100 nm thick) showed the high density of particles but only some rare folded fibrils (marked by dotted line) were seen on Fig. 3D. (H-J) Surface rendering and rotation of some sub-volumes performed within the cluster of particles at high magnification showed only rare folded fibrils. Scale bars, 500 nm.

FIGURE 4: Electron tomography reveals the distribution of UBTF1-GFP as elongated folded fibrils in FC of pre-segregated FC (AMD treatment for 1h). (A-C) 3D visualization and rotation of one tomogram evidenced that each large FC was constituted by the gathering of several FCs identified by clusters of particles (outlined by white lines). (D-G) 100 nm thick sub-volumes were cut from the tomogram and maximum intensity projection (MIP mode) was applied in different directions. The folded and looped fibrils (marked by dotted lines) are evidenced in all directions. (H-K) Surface rendering and rotation of some sub-volumes performed within the cluster of particles at high magnification evidenced more clearly the presence of numerous folded and looped fibrils. To note: the same results were found for UBTF2-GFP (see fig S 8). Scale bars, 500 nm.

FIGURE 5: Electron tomography reveals the distribution of UBTF1-GFP and UBTF2-GFP as long folded fibrils in nucleolar caps induced by AMD treatment for 2h. (A-H) Concerning UBTF1-GFP, 3D visualization and rotation of one tomogram evidenced that each cap contained several clusters of particles (outlined with white lines in A and B). (C) Axial virtual section cut in the tomogram shows the presence of folded and looped fibrils. (D-H) Surface rendering and rotation of some sub-volumes performed at higher magnification evidenced more clearly the presence of numerous folded and looped fibrils. (I-L) Concerning UBTF2-GFP, 3D visualization and rotation of one tomogram confirmed the presence of several clusters of particles within each cap (outlined with white lines in I). (J) Axial virtual section cut in the tomogram shows the presence of folded and looped fibrils which were confirmed in 3D visualization (K and L). Scale bars, 500 nm.

FIGURE 6: Electron tomography reveals the distribution of UBTF1-GFP as long folded fibrils in all mitotic NORs. (A) In doubly transfected cells expressing histone H2B-GFP and UBTF2-DsRed, confocal imaging and 3D reconstruction of structures containing UBTF2-DsRed identified mitotic NORs of different sizes: small (# 1-4), medium (# 5-7) and large (# 8, 9). (B) In transfected cells expressing UBTF1-GFP, pre-embedding nanogold labeling of GFP imaged in a thick section by electron microscopy evidenced two medium sized mitotic NORs (arrows) within the metaphase plate (chr; limited with the dotted line). (C)

Two mitotic NORs arrowed on B were visualized in 3D after electron tomography. (D-G) 3D visualization and rotation at high magnification of one mitotic NOR showing that particles were distributed as folded and looped fibrils**.** (H-I) One 100 nm thick sub-volume was cut from the tomogram and maximum intensity projection (MIP mode) was applied. It evidenced folded fibrils (arrows) whose pattern of packing was similar to those visualized in FCs of control and AMD treated cells. The sub-regions of the NOR localized within the upper and lower rectangles on H correspond to those in the upper and lower left circles respectively on D-G. The sub-region limited with the rectangle in I corresponds to that in the lower right circle on G. Scale bars: 5 µm (A, B), 500 nm (C), 100 nm (D-G), 200 nm (H, I).

FIGURE 7: Electron tomography reveals the distribution of UBTF2-GFP as long folded fibrils in all mitotic NORs. (A) Imaging of UBTF2-GFP by electron microscopy evidenced small, medium and large mitotic NORs (arrow). (B) Large NOR, arrowed on A, visualized in 3D after electron tomography contained several sub-regions separated with loosened areas (circles). (C-F) Surface rendering and rotation of the loosened areas evidenced looped fibrils (circle). (G) 100 nm thick sub-volumes were cut from the tomogram to study the region circled on C and E and maximum intensity projection (MIP mode) was applied. This procedure revealed numerous looped fibrils disposed in different directions (arrows in rectangle). (H-K) The same procedure was applied on the region in the upper circle on B: it revealed numerous looped fibrils in all directions (arrows in and out of circle). Scale bars: 5 µm (A), 500 nm (B), 250 nm (C, G and I-K), 100 nm (D-F), 200 nm (H).

FIGURE 8: Our new model proposes that an active rRNA gene is organized as a globular structure or *r-Chromatin Globule* (r-CG). In this figure, we describe the different steps that are necessary to organize an extended active rDNA gene in a globular structure located in one fibrillar center (FC). (A) A spread rDNA repeat presented at scale shows (from left to right) one IGS in red, one enhancer in purple, one transcribed unit with 100 associated Pol I molecules, one terminator in blue and next IGS in red. (B-E) The two IGS flanking the transcription unit are condensed and gathered. This induces the transcribed region to organize as four extended loops and the enhancer and terminator sequences to constitute uncondensed loops grouped as a central core. (F-J) In the next steps, the 4 extended loops strongly fold to constitute 4 separate shorter coils that bend around enhancer and terminator loops. (K) Final 3D conformation of one rDNA gene located within one FC, around 0.3 to 0.4 µm in diameter, is shown without growing rRNA molecules. (L-N) Pre-rRNA molecules are drawn as growing green threads oriented towards the periphery of the rDNA globule. (O-Q) Growing rRNA constitute one part of dense fibrillar component drawn as transparent green curved tubes whereas the rDNA gene associated to Pol I molecules is organized as coils located in the cortex of FC. Scale bars: 1 µm (A-C), 500 nm (D, E), 250 nm (F), 150 nm (G-L).

Supplementary Figure Legends

Supplementary Figure 1 In cells expressing UBTF1-GFP and UBTF2-GFP, confocal imaging evidences that AMD treatment induces similar changes in number, shape, structure and size of sites containing UBTF1-GFP and UBTF2-GFP. (A-F) localization of UBTF1-GFP in (A, B) control cells, in (C, D) cells treated with AMD for 1 h (pre-segregated nucleoli) and (E, F) cells treated with AMD for 2 h (segregated nucleoli). (G-L) localization of UBTF2-GFP in (G, H) control cells, in (I, J) cells treated with AMD for 1 h (pre-segregated nucleoli) and (K, L) cells treated with AMD for 2 h (segregated nucleoli). AMD provokes similar changes both in the structure of the nucleolus and in the localization of UBTF1-GFP and UBTF2-GFP isoforms. Note, in pre-segregated nucleoli, that gathering of fluorescent spots resulted in their diminution and their enlargement within the nucleolar territory. In contrast, in segregated nucleoli,

fluorescent areas migrated to the nucleolar periphery and are transformed in caps. Comparison with phase contrast images allowed the precise localization of fluorescent caps (arrows) relatively to nucleolar structures. Scale bars: 5 µm (A-D), 4 µm (E-F), 7.5 µm (G-H), 4 µm (I-J), 4.5 µm (K-L).

Supplementary Figure 2 Confocal imaging reveals that UBTF1 and 2 are co-localized in control cells and in cells treated with AMD for 1 and 2 h. (A-F) In control cells UBTF1-GFP and UBTF2-GFP (A and D) are localized in numerous bright spherical foci disposed as beads on a string. The same cells labeled with a monoclonal antibody raised against GFP revealed with a Texas Red conjugated secondary antibody (B and E) demonstrated that the anti GFP antibody was strictly co-localized with UBTF1-GFP or UBTF2-GFP. (G-U) Doubly transfected cells expressing UBTF1-GFP and UBTF2-DsRed or UBTF1-DsRed and UBTF2-GFP proteins demonstrated strict co-localization of both isoforms in (G-I and P-R) control cells, in (J-L) cells treated with AMD for 1h and (M-O and S-U) cells treated with AMD for 2h. Scale bars: 6 µm.

Supplementary Figure 3 Ultrathin sections imaged by electron microscopy revealed similar distribution of UBTF1-GFP within FC of different nucleoli of control cells or within the same FC observed on serial sections. (A-C) In small and medium FCs (outlined by white circles) numerous particles are grouped in several clusters measuring 60 to 100 nm in diameter frequently elongated and either linear (200 nm long) or curved (300 nm long). Around these clusters individual particles are absent. Some particles were found within nucleolar vacuoles (NV) or interstices. No particles were found within the dense fibrillar component (dfc) and granular component (gc). Rare particles were found within the nucleoplasm (N) and condensed chromatin (chr). (D-F) Three serial sections (not successive) of one nucleolus, showing the same distribution of particles as clusters 60 to 100 nm in diameter within the whole volume of a large FC (outlined by white circle). C: cytoplasm; N: nucleoplasm; NE: nuclear envelope; nl: nucleolus; NV: nuclear vacuoles. Scale bars, 1 µm.

Supplementary Figure 4 Ultrathin sections imaged by electron microscopy revealed similar distribution of UBTF1-GFP within FC of different nucleoli of cells treated with AMD for 1 or 2 h or within the same FC observed on serial sections. (A-C) In numerous enlarged FCs, particles are grouped in several clusters measuring 60 to 100 nm in diameter. (D-F) Three serial sections (not successive) of one pre-segregated nucleolus at higher magnification displaying the distribution of the label through the depth of enlarged FCs (fc). Particles were frequently grouped as clusters 60 to 100 nm in diameter as in control cells, but a lot of individual particles were also distributed along fibrils (arrow on F). (G-I) In segregated nucleoli, particles were no longer found as clusters, but as single particles distributed as curved fibers (arrows on H). The dotted lines on H and I mark the limit between FCs and the RNP part of the residual nucleolus. C: cytoplasm; N: nucleoplasm; NE: nuclear envelope; nu: nucleolus; NV: nuclear vacuoles. Scale bars, 1 µm.

Supplementary Figure 5 Ultrathin sections imaged by electron microscopy revealed similar distribution of UBTF2-GFP within FC of different nucleoli of control cells or within the same FC observed on serial sections. (A-B, C-E and F-G) In two serial sections (A-B), in three serial sections (C-E) and in two serial sections (F-G) of different nucleoli, small and medium FCs (circles) revealed numerous particles homogeneously dispersed. Large FC revealed that, in contrast to UBTF1-GFP, particles identifying UBTF2-GFP were not grouped as clusters but distributed at random. (H) Within very large FC, particles were present in the cortical part of FCs but were absent in the central part. Some particles were also found within nucleolar vacuoles (NV) and were rare in other nucleolar components. Some

particles were also found in nucleoplasm and condensed chromatin. C: cytoplasm; N: nucleoplasm; NE: nuclear envelope; nu: nucleolus; NV: nuclear vacuoles. Scale bars, 1 µm (A-G); 0.5 µm (H).

Supplementary Figure 6 Ultrathin sections imaged by electron microscopy revealed similar distribution of UBTF2-GFP within FC of different nucleoli of cells treated with AMD for 1 or 2 h or within the same FC observed on serial sections. (A, B) Two serial sections (not successive) of one pre-segregated nucleolus showing the distribution of particles within five enlarged FCs (fc); (C-E) Two nucleoli showing large FCs. In all these examples, particles were not distributed at random but were frequently aligned as curved fibrils (dotted line). (D) Area limited with a rectangle in C observed at higher magnification. (F, G) Two fully segregated nucleoli exhibiting large crescent-like caps (circle on F) adjacent to the surface of the residual RNP part. Particles were very numerous and disposed at random or as curved fibrils. Dotted lines mark the limit between cap and DFC. C: cytoplasm; N: nucleoplasm; NE: nuclear envelope; nu: nucleolus; NV: nuclear vacuoles. Scale bars, 0.5 µm.

Supplementary Figure 7 Examples illustrating the different steps in the processing of tomograms and in the extraction of sub-volumes to study the 3D distribution of particles identifying UBTF1/2-GFP. (A) Surface rendering reveals the global repartition of particles. (B, C) Different 100 nm thick sub-volumes were cut from the tomogram. The distribution of particles contained within these sub-volumes was investigated by using either maximum intensity projection mode on different orthogonal planes and/or 3D visualization (surface rendering mode)**.** (D, E) To study the distribution of particles more precisely, orthogonal or oblique sections can be cut in different orientations. (F, G) The contour of fibrils can be outlined by hand to increase their visualization; circles identify areas in which looped fibrils were obvious. (H, L) 3D visualization (surface rendering mode) and rotation in different directions demonstrated looped fibrillar structure within the sub-volume.

Supplementary Figure 8 Electron tomography reveals the distribution of UBTF2-GFP as elongated folded fibrils in FC of pre-segregated FC (AMD treatment for 1h). (A-C) 3D visualization and rotation of one tomogram evidenced that each large FC was constituted by the gathering of several FCs identified by clusters of particles (outlined by white lines). (D-G) 100 nm thick sub-volumes were cut from the tomogram and maximum intensity projection (MIP mode) was applied in different directions. The folded and looped fibrils (marked by dotted lines) are evidenced in all directions. (H-L) Surface rendering and rotation of some sub-volumes at high magnification evidenced more clearly the presence of numerous folded and looped fibrils. Scale bars, 500 nm.

Supplementary Figure 9 Electron tomography reveals the same as in KB cells distribution of UBTF1-GFP (Fig. X1 A-F) and UBTF2-GFP (Fig. X1 G-M) as coils and loops in FC of control A549 cells (compare with Fig 2 and 3). (A, B) 3D visualization and rotation of UBTF1-GFP positive FC evidenced that particles were distributed along fibrils that are organized as coils and loops. (C-F) 100 nm thick sub-volumes were cut from the tomogram (shown on Fig. X1 A, B) at different depth of axial plane; MIP mode was applied for better visualization of UBTF-GFP positive fibrils. The loop like folding of fibrils is clearly visible. (G, H) 3D visualization and rotation of UBTF2-GFP positive FC. UBTF2-GFP positive fibrils are organized in same manner as UBTF1-GFP fibrils, forming well recognizable coils and loops. (I-K) For better demonstration of fibrils that organize UBTF2-GFP positive FC we performed MIP mode of 100 nm thick sub-volumes that were cut from the tomogram (shown on Fig. X1 G, H) at different depth of axial plane; the loop like folding of UBTF2-GFP fibrils is clearly pronounced. (L, M) Parts of fibrils isolated from the interior of the sub-volume presented on Fig. X1 I-K were visualized at higher magnification in 3D and rotated to evidence their folding and bending. Scale bars: 75 nm (A-H); 150 nm (I-K); 80 nm (L, M).

Supplementary Figure 10 Electron tomography displaying the distribution of UBTF1-GFP (Fig. X2 A-F) and UBTF2-GFP (Fig. X2 G-L) in enlarged FCs extracted from pre-segregated nucleoli of A549 cells treated with AMD during 1h. Note the same organization of elongated and folded in loop-like fashion fibrils forming FC as it was demonstrated in pre-segregated nucleoli of KB cells (compare with Fig. 4 and Fig. S8). (A-C) 3D visualization and rotation of one tomogram UBTF1-GFP positive FC evidenced that each enlarged FC was constituted by the gathering of several FCs identified by clusters of particles (outlined by red lines). (C-D) 100 nm thick sub-volumes were cut from the tomogram and MIP mode was applied at different depth. The folded and looped fibrils are evidenced in both planes demonstrated. Red lines on Fig. X2 C, D outline clusters of particles that correspond to one smaller FC, shown in the upper right and upper left corners on Fig. X2 A and Fig. X2 B respectively. (E, F) Surface rendering and rotation of some sub-volumes performed within the cluster of particles taken in black rectangle on Fig. X2 C at high magnification evidenced more clearly the presence of numerous folded and looped fibrils. (G-L) The same results were found for UBTF2-GFP. Images on Fig. X2 I, J represent 100 nm sub-volumes cut from clusters outlined by white rectangles on Fig. X2 G, H). Scale bars: 150 nm (A-D; G-J); 85 nm (E, F, K, L).

Supplementary Figure 11 Electron tomography reveals the distribution of UBTF2-GFP as long folded fibrils in cap of segregated nucleolus of A549 cells (caps were induced by AMD treatment for 3h). (A) 3D visualization of one tomogram evidenced the presence of several clusters of particles within each cap (outlined with red lines. (B, C) Axial virtual sections cut from the tomogram shown on Fig. X3 A display the presence of folded and looped fibrils. (D) Surface rendering and rotation of some sub-volumes performed at higher magnification evidenced more clearly the presence of numerous folded and looped fibrils. Red lines outline several clusters of particles; most probably they correspond to distinct FCs fused into cap-like structure. (E) 100 nm thick sub-volumes were cut from the tomogram shown on Fig. X3 D; MIP mode projection was performed at different depth. The folded and looped fibrils are obvious. Red line outline clusters of particles that correspond to one smaller FC, shown in the lower middle part of the previous image. (F, G) 3D visualization and rotation of tomogram extracted from the depth of the volume presented on fig X3 D confirmed the presence of folded and looped fibrils. Scale bars: 650 nm (A-C); 270 nm (D, E); 100 nm (F, G).

Supplemental movie 1

In this movie we show the successive steps to wrap a spread rDNA in 3D. At the beginning of the movie, one spread rDNA repeat is first drawn at scale. It shows (from left to right) one IGS in red, one enhancer in purple, one transcribed unit with 100 associated Pol I molecules, one terminator in blue and next IGS in red. On next sequences we propose successive steps needed to wrap this spread rDNA in 3D in order to finally position it within one FC with the constraint of maintaining its uncondensed state. In a first step, the two IGS flanking the transcribed unit are condensed and gathered. Enhancer and terminator are maintained as uncondensed loops that are grouped as a central core around which the transcribed region constitutes four extended loops. In the next steps, these 4 loops strongly fold to constitute 4 separate shorter coils that bend around enhancer and terminator loops. Finally, growing pre-rRNA molecules are drawn as green threads ended with a terminal knob at their 5' end that directly enter surrounding DFC (transparent green curved tubes).

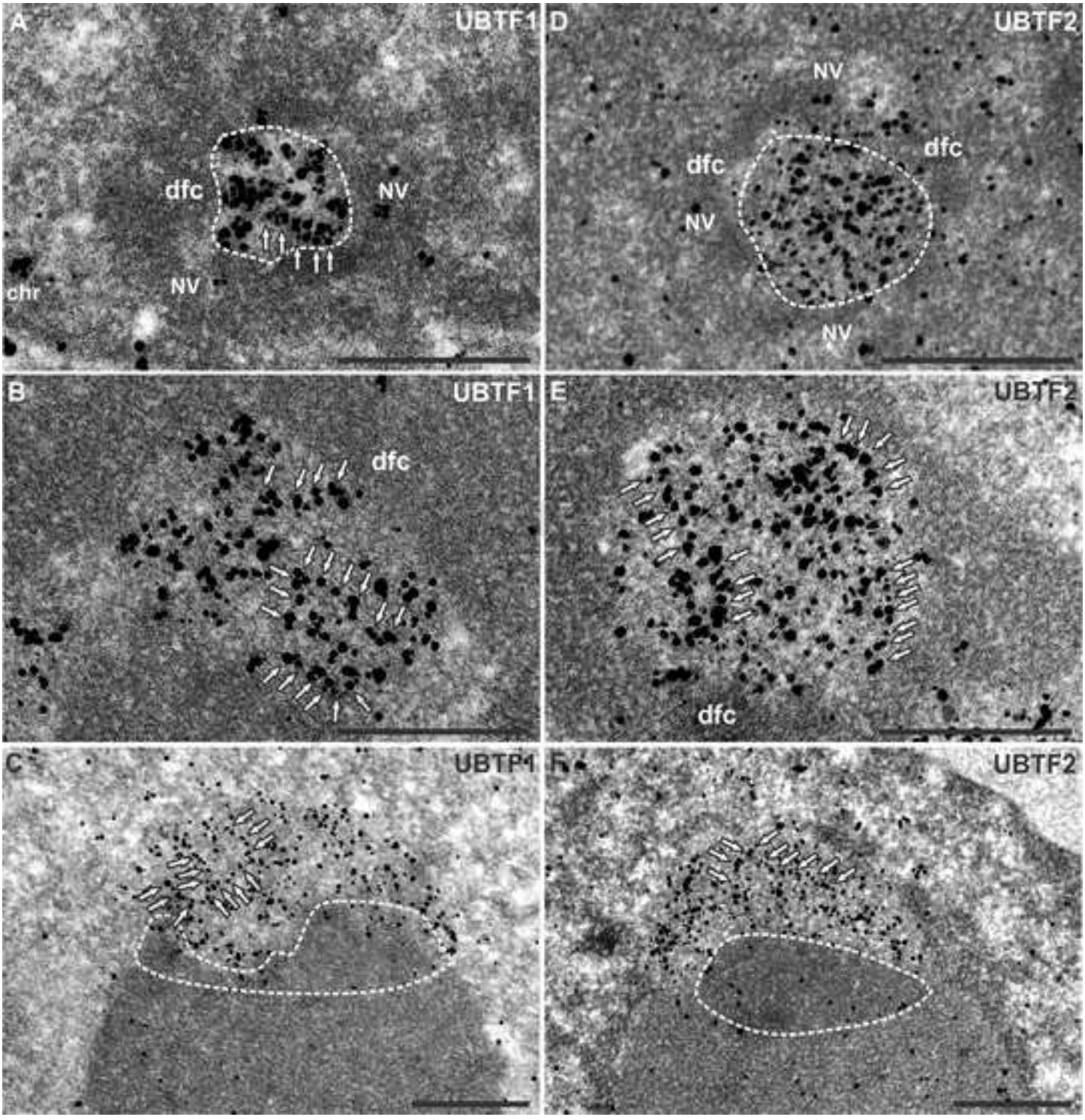
A
UBTF1
dfc
NV
chr
NV
D
UBTF2
NV
dfc
dfc
NV
NV
B
UBTF1
dfc
E
UBTF2
dfc
C
UBTF1
F
UBTF2

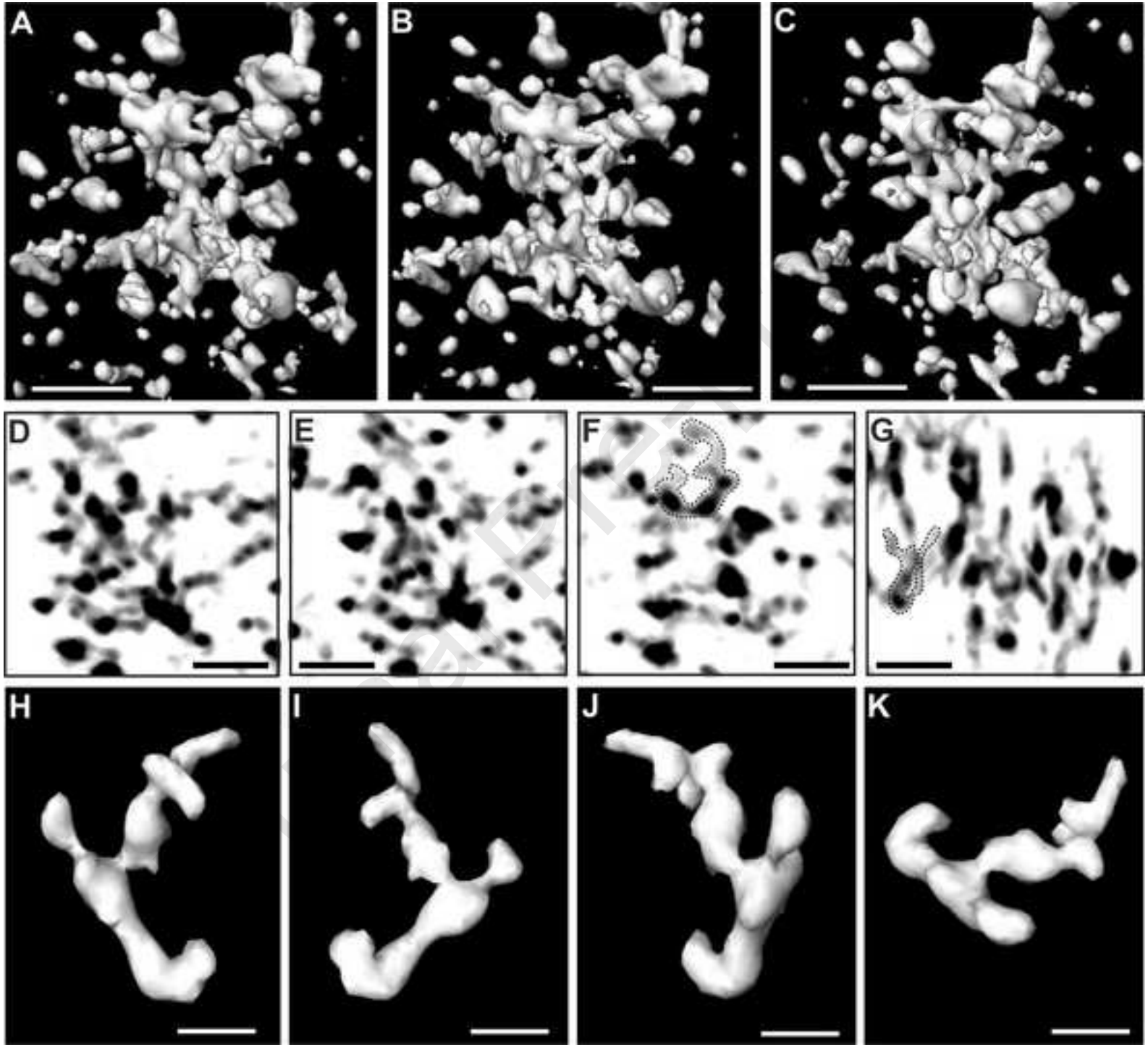
A
B
C
D
E
F
G
H
I
J
K

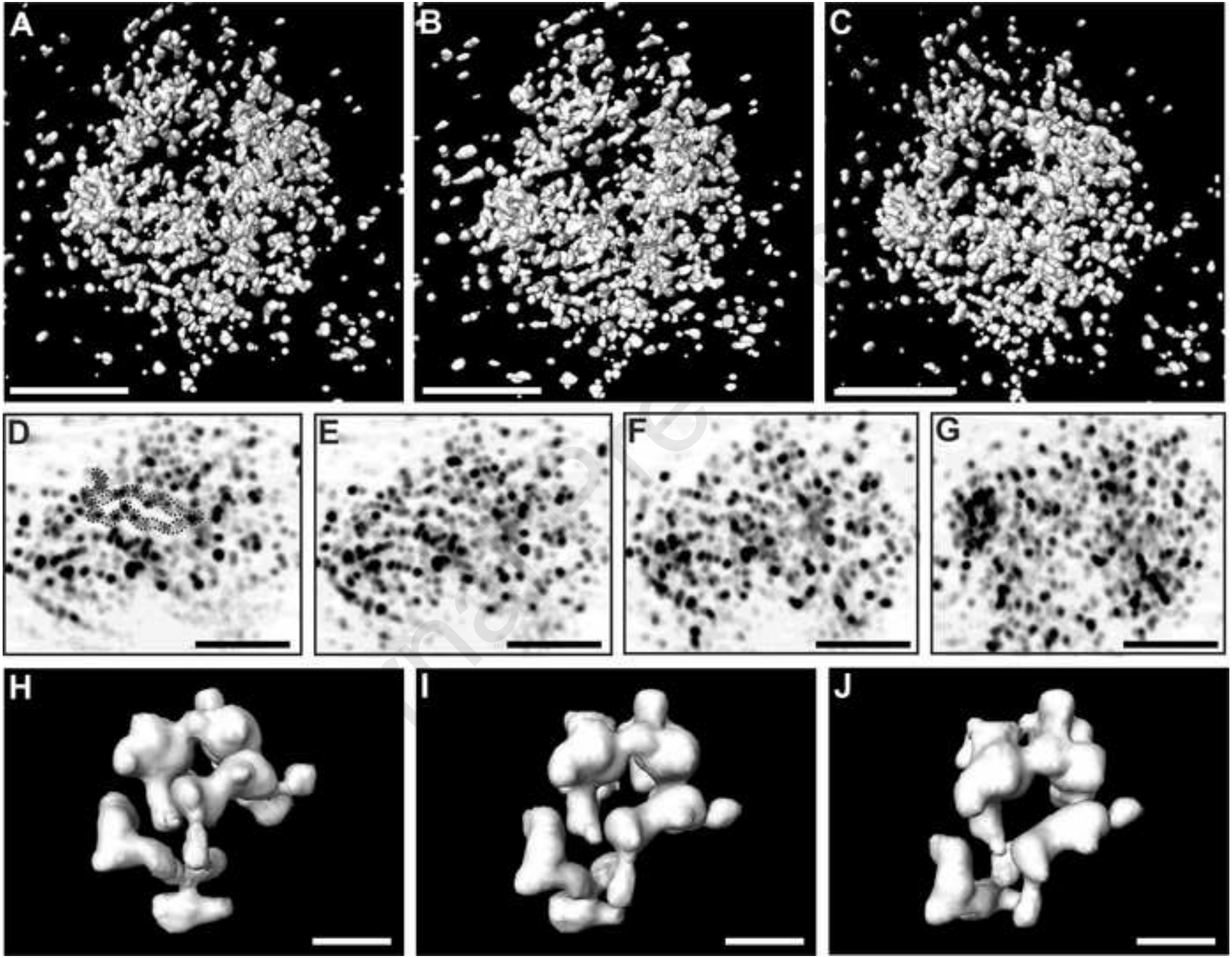
A
B
C
D
E
F
G
H
I
J

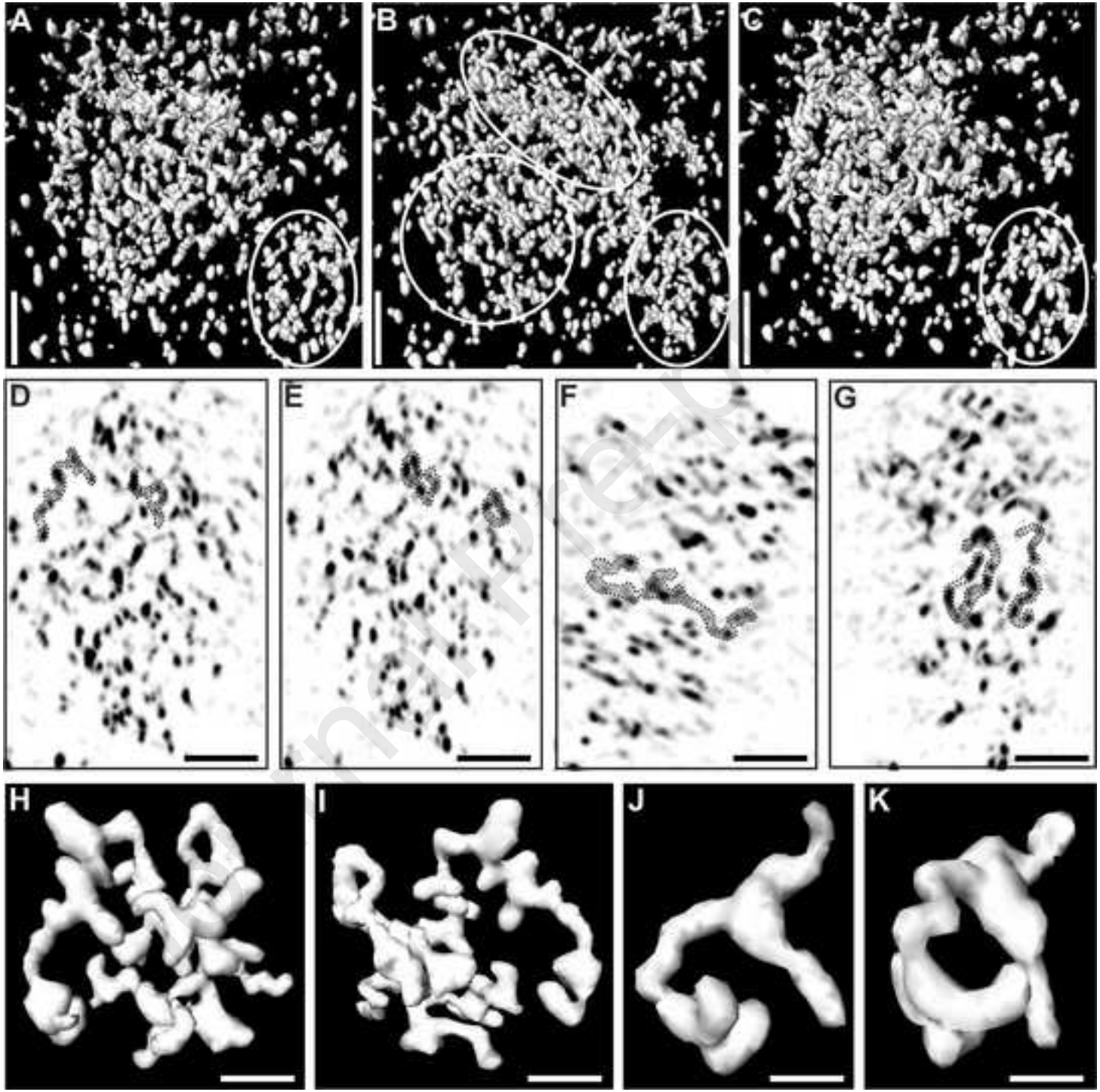
A
B
C
D
E
F
G
H
I
J
K

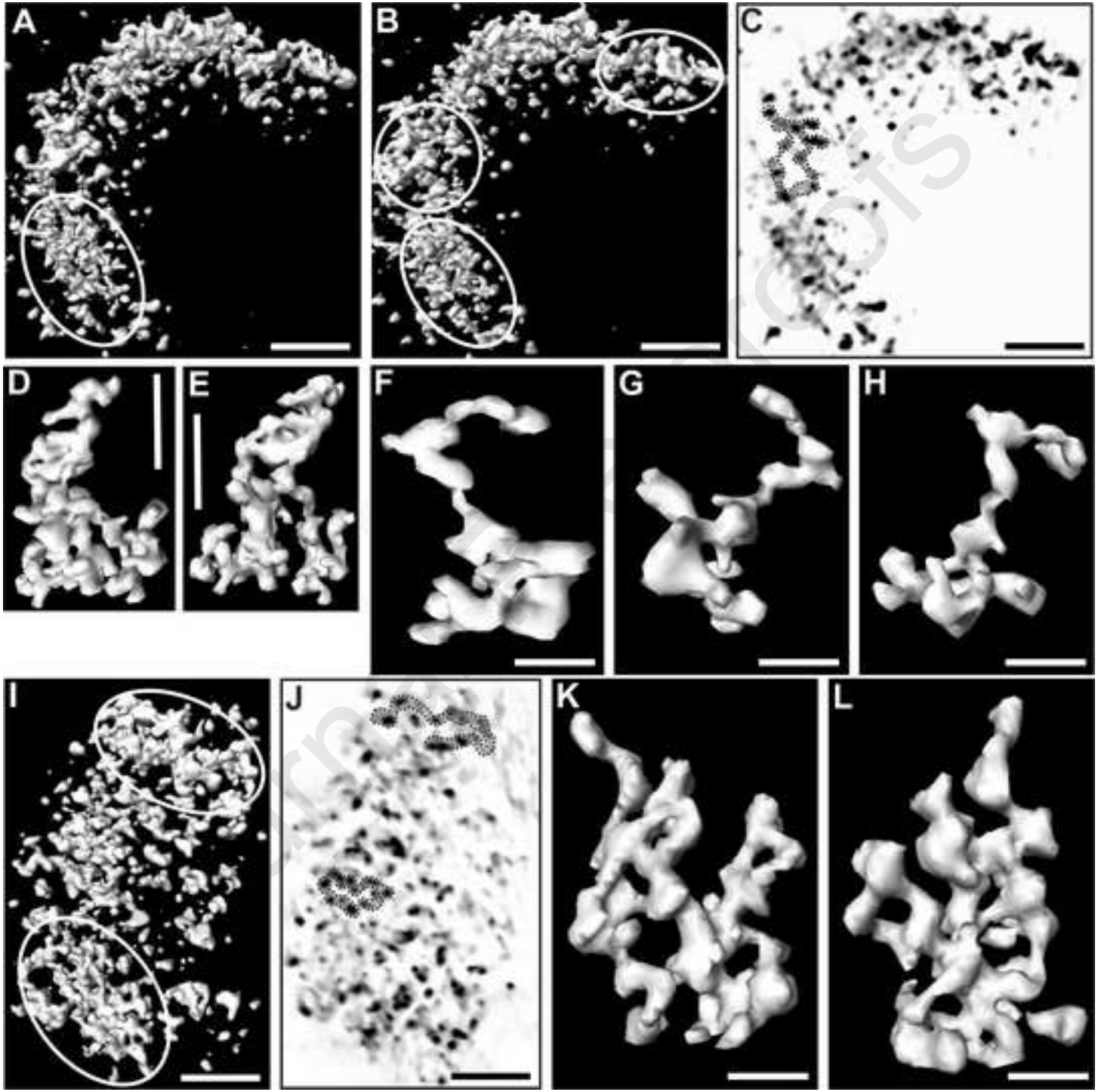
A
B
C
D
E
F
G
H
I
J
K
L

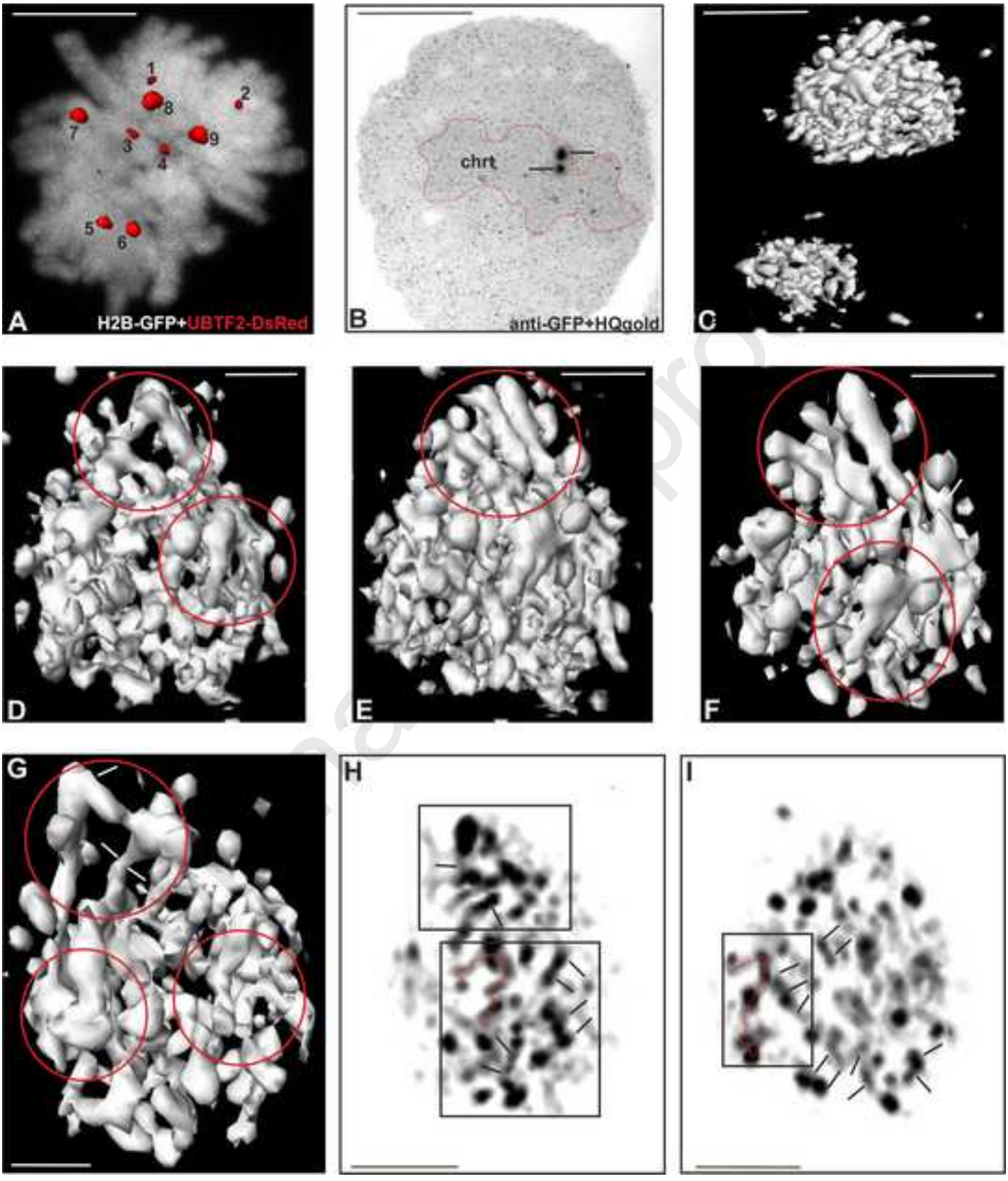
A
H2B-GFP+UBTF2-DsRed
1
2
3
4
5
6
7
8
9
B
chrt
anti-GFP+HQgold
C
D
E
F
G
H
I

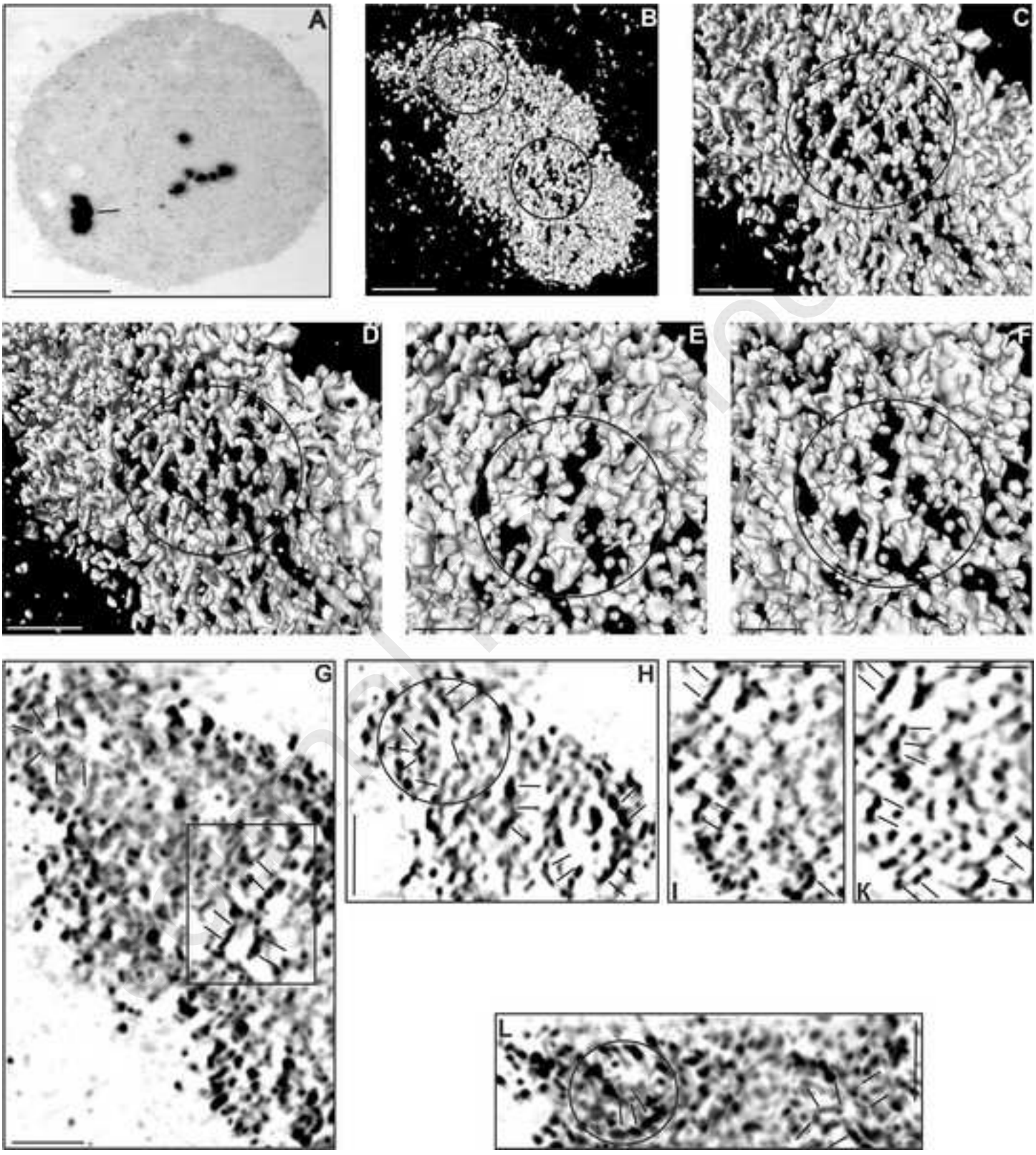
A
B
C
D
E
F
G
H
I
K
L

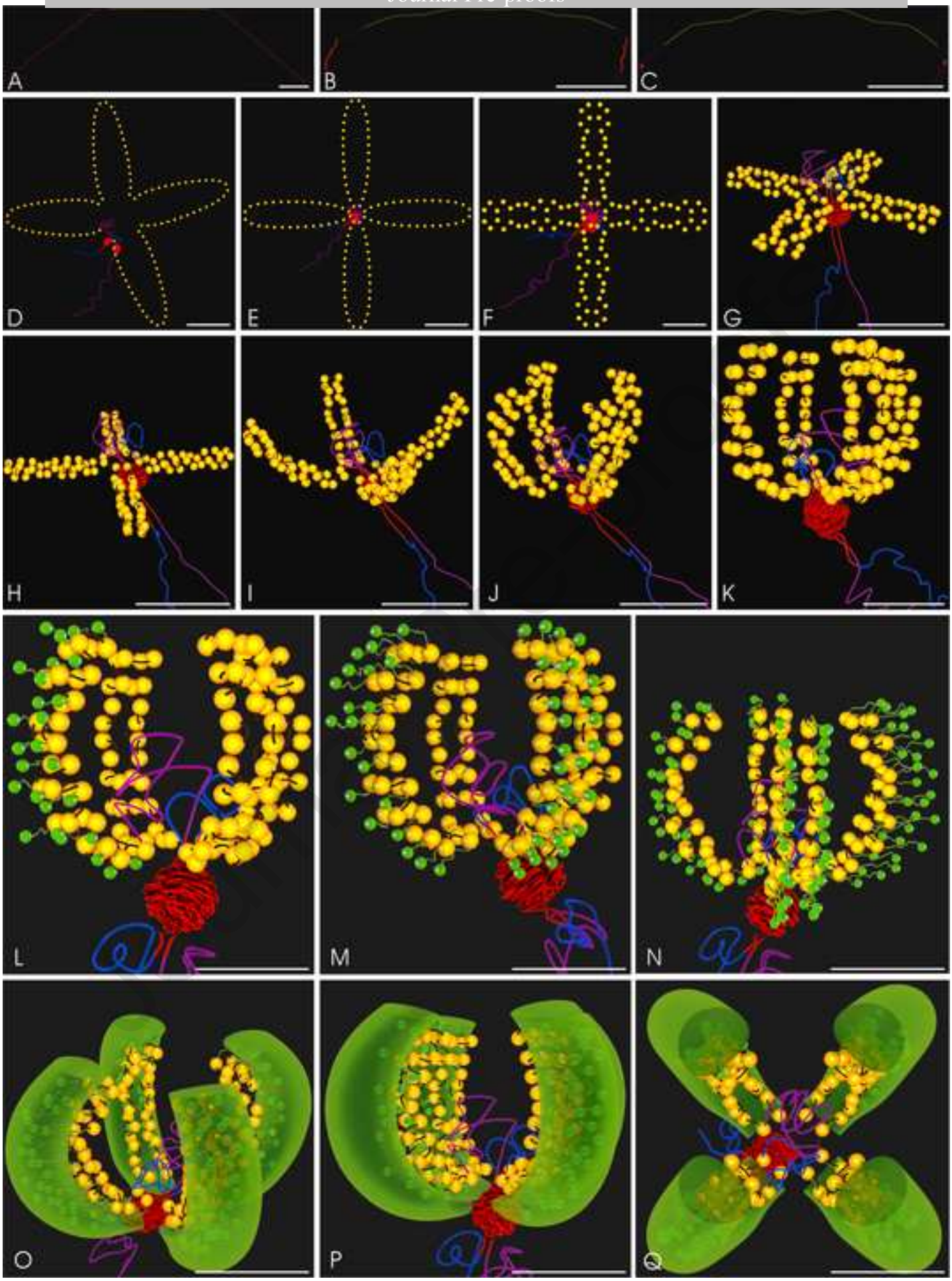
A
B
C
D
E
F
G
H
I
J
K
L
M
N
O
P
Q

Graphical abstract

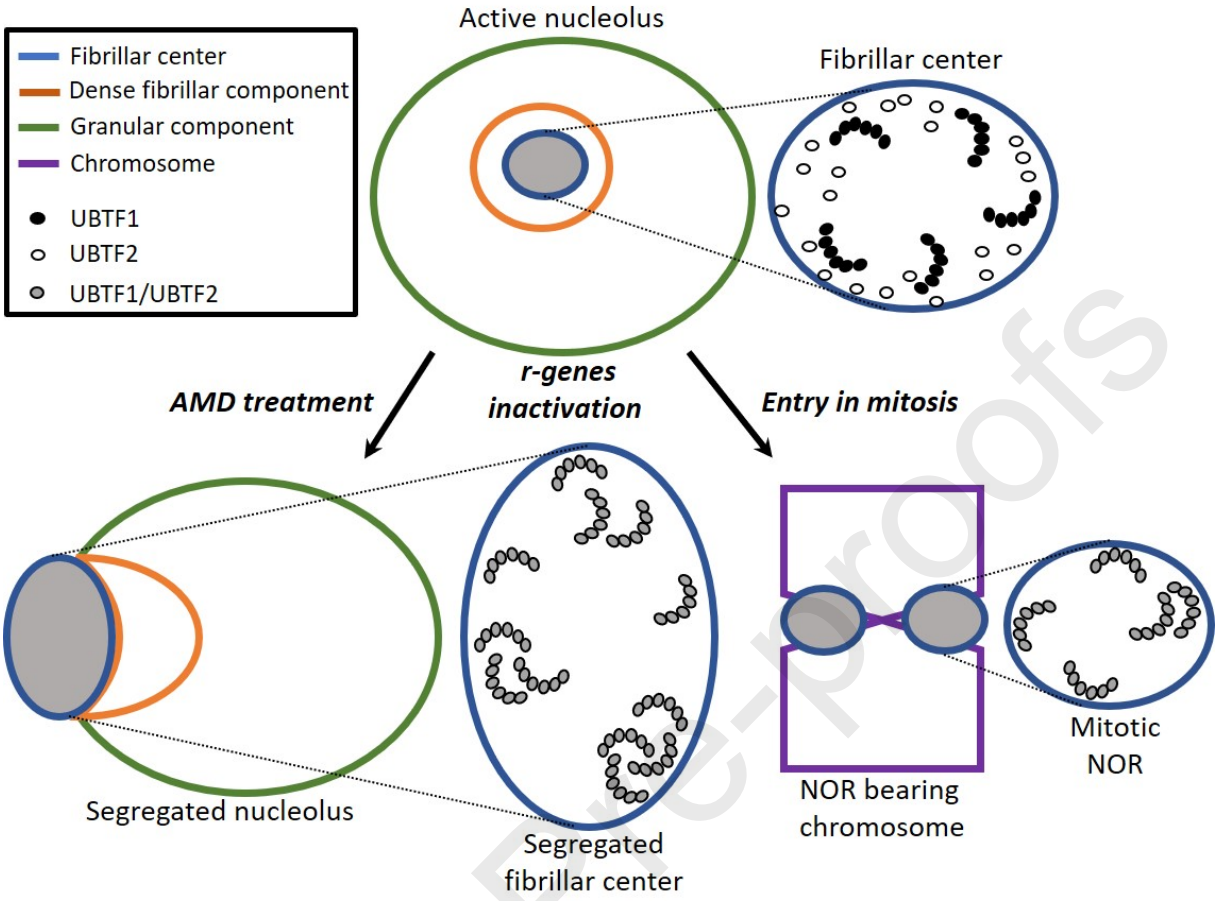

Electron Tomography Reveals Changes in Spatial Distribution of UBTF1 and UBTF2 Isoforms within Nucleolar Components during rRNA Synthesis Inhibition

- Both UBTF isoforms are distributed and organized differently within nucleolar FC
- Results are included into a model of 3D organization of active transcribing r-gene
- Similar distribution of both isoforms is observed when rRNA synthesis is inhibited
- Roles for both variants are suggested in the organization of active/inactive r-genes